Low pressure gas transfer in fibrous media with progressive infiltration: correlation between different transfer modes

Carole Charles[a,b], **Cédric Descamps**[c,a], **Gerard L. Vignoles**[a]

[a]*University of Bordeaux,*
Laboratory for ThermoStructural Composites (LCTS)
UMR 5801: CNRS-Safran-CEA-U. Bordeaux
3, Allée de La Boétie, 33600 Pessac, France
[b]*ArianeGroup, 3 rue de Touban, 33185 Le Haillan, France*
[c]*Safran Ceramics, 105 avenue Marcel Dassault, 33700 Mérignac, France*

Abstract

Permeation of gases in fibrous preforms of C/C composites has been studied with various degrees of infiltration, between 60% and 12% pore volume fraction, both experimentally with steady-state flow *vs.* pressure drop experiments and numerically with X-ray computerized micro-tomography (μ-CT), image processing and image-based computations. An excellent agreement has been found for Darcian permeabilities and for Knudsen diffusivities, when taking the mean solid chord length as a characteristic length scale. The reported tendencies of the mass transfer coefficients *vs.* porosity are in agreement with fibrous filters literature values, that are available for pore volume fractions above 55%. Accordingly, this work proposes useful extensions of these known correlations towards lower values of porosity. Finally, the dimensionless friction factors related to Knudsen diffusion, binary diffusion and viscous flow have been found to be correlated between each other, regardless the flow direction or the type of fibrous media. They are easy-to-use tools for large-scale numerical simulations of mixed-mode gas flow, *eg.* in Chemical Vapor Infiltration (CVI) or filter clogging simulations.

Keywords: Fibrous media; Rarefied gas transfer; Permeability; Image-based

modeling

---

1. Introduction

Rarefied gas transfer in fibrous media is involved in numerous applications : air filtering and sanitization [1–5], Gas Diffusion Layers (GDL) in fuel cells [12, 13], Thermal Protection Systems (TPS) ~~by~~based on fibrous felts [6–10], as well as the manufacturing of polymer-matrix composite materials [11] by liquid resin infiltration and ceramic-matrix composites by Chemical Vapor Infiltration (CVI) for [14–16].

For the applications mentioned above, it is of great interest to predict the permeability or gas diffusivity of a ~~preform~~fibrous medium from its microstructure ~~(porosity, pore diameter, internal surface area)~~. The behavior of gas flow through porous media ~~in closely related families~~ ~~are~~ generally follows ~~similar~~the same type of laws, but the diversity of these material structures (with variable fiber diameter, woven or unwoven, ordered or randomly oriented fibers, 1D, 2D or 3D arrangements, . . .) makes it difficult to have a common model for the transport coefficients [17].

For instance, in the CVI process, an optimal densification depends on the competition between mass transport, which depends on diffusive and convective flows, and heterogeneous reactions kinetics, which themselves depend on the internal surface area [18]. The case of CVI is of particular interest since it features an evolving porous medium, in which the starting configuration looks like a fibrous filter but progressively changes towards a medium with very low porosity and permeability. This is also the case of filters when they get progressively clogged by the deposition of dust particles. In that situation it is necessary to provide estimates of the geometrical and transport properties over the whole range of porosity [2].

Experimentally, permeability coefficients are classically obtained by steady-state measurements of the pressure drop for controlled flow rates taking slip-flow effects [4, 7, 9] into account or not [19–22]. Some values are obtained by transient (*i.e.* pressure-pulsed) methods [23, 24]. ~~For instance,~~ Hou *et al.* also used transient methods, taking gas slip effects into account [25].

Due to the variety of fibrous structures, a large amount of data and models are available for viscous flow permeabilities [7]. Comparatively fewer data are available in the rarefied regime, *ie.* for pore diameters smaller than the molecular mean free path, except in the case of fibrous filters, with low solid volume fractions (SVF). Even though correlations are available, the scarcity of experimental data used for their validation still leaves some uncertainty in using them when applied to porous media which are not exactly the ones used for their construction.

Tomadakis & Robertson [26] have applied an interesting correlation between ordinary diffusion and viscous permeability on a family of porous media with evolving porosity [27]. A correlation exists between Knudsen transport resistance and viscous transport resistance in the case of fibrous filters [4], but its generality is still an open question.

Transport coefficients related to viscous flow, slip-flow (or rarefied gas flow) and ordinary diffusion can be cast into non-dimensional~~In terms of~~ tortuosity factors $\underline{\underline{\eta}}_v$, $\underline{\underline{\eta}}_K$ and $\underline{\underline{\eta}}_b$, respectively. However, there is no reason for them to be equal to each other [28] and there is a lack of correlation between all flow regimes in the literature. Correlation between the three tortuosities could be interesting to see how the three kinds of gas transfer ~~evoluate~~relate to each other.

In this work, we will present a systematic study of rarefied gas flow permeation in C_f/C composites (which belong the family of ceramic-matrix composites) during their preparation, either by CVI or by liquid polymer infiltration. These composites ~~which~~ are ~~needled~~ fibrous media (often called “preforms”) progressively infiltrated by a matrix. The study developed here ~~, that~~ involves experimental steady-state flow/pressure drop measurements as well as image-based computations making use of X-ray CT scans of the media. The objective is to produce correlations that are as much as possible validated experimentally.

After recalling some elements about continuum to rarefied gas transfer in porous media and performing a survey of previous models and correlations, we will describe the numerical and experimental approach used here. Then, the results will be presented and compared to existing literature. Finally, some original correlations will be proposed.

2. Useful definitions for low pressure gas transfer

2.1. Pure gas flow in rarefied and continuum regimes

For a pure gas, there are several flow and diffusion regimes, as determined by the Knudsen number Kn, defined by the ratio between the molecule mean free path $\langle\lambda\rangle$ and the mean intercept length $\langle\ell\rangle$, which corresponds to the average distance between two ~~pore walls~~contiguous interfaces, usually equivalent to a mean pore diameter $\left\langle d_p\right\rangle$ or to a mean fiber diameter $\left\langle d_f\right\rangle$.

$$Kn = \frac{\langle\lambda\rangle}{\langle\ell\rangle} \tag{1}$$

The mean free path corresponds to the average distance traveled by a molecule between two successive collisions with another molecule. It depends on several parameters, as described by the kinetic theory of gases :

$$\langle\lambda\rangle = \frac{k_B T}{\sqrt{2}\pi d_m^2 P} \tag{2}$$

Where k_B is the Boltzmann constant, T the temperature, d_m the gas molecular diameter and P the pressure.

For very high Knudsen numbers, in isothermal conditions, a free-molecule gas flow $\mathbf{j}_K$ (kg.m^{-2}.s^{-1}) takes place through a permeable porous medium when a density gradient $\nabla\rho$ occurs. In a single pore one has :

$$\mathbf{j}_K = -\mathcal{D}_K \nabla\rho \tag{3}$$

where the Knudsen diffusion coefficient is introduced as :

$$\mathcal{D}_K = \frac{1}{3}\langle c\rangle \cdot d_p \tag{4}$$

in which the average molecular velocity is given by:

$$\langle c\rangle = \sqrt{\frac{8\mathcal{R}T}{\pi M}} \tag{5}$$

In a complex porous medium, relation (3) is easily extended as :

$$\mathbf{j}_K = -\underline{\underline{\mathcal{D}}}_K \nabla\rho \tag{6}$$

where the tensorial Knudsen diffusivity is given by :

$$\underline{\underline{\mathcal{D}}}_K = \varepsilon \underline{\underline{\eta}}_K^{-1} \frac{1}{3}\langle c\rangle \left\langle d_p \right\rangle \tag{7}$$

in which a contribution of the porosity ε appears for obvious reasons of limited fluid accessibility and where a Knudsen tortuosity tensor represents a possibly anisotropic contribution of the porous medium geometry.

On the other hand, when the Knudsen number is very low, the flow is linked to the fluid viscosity. In a single pore, one has the Poiseuille relationship :

$$\mathbf{j}_\nu = -\nu^{-1} K \nabla P \tag{8}$$

where $K = d_p^2/32$ is the permeability and the the kinematic viscosity ν is closely related to the self-diffusion coefficient :

$$\nu = \mu\rho^{-1} \approx \mathcal{D} = \frac{1}{3}\langle c\rangle\langle\lambda\rangle\,. \tag{9}$$

Generalizing eq. (8) to a porous medium gives Darcy's law :

$$\mathbf{j}_\nu = -\nu^{-1}\underline{\underline{K}}\nabla P \tag{10}$$

where the permeability tensor is :

$$\underline{\underline{K}} = \varepsilon\underline{\underline{\eta}}_\nu^{-1}\frac{\left\langle d_p\right\rangle^2}{32} \tag{11}$$

These two transport modalities act in parallel to each other, that is, the total mass flux is the sum of the Knudsen and viscous contributions. Using the perfect gas law, one has :

$$\mathbf{j}_{tot} = \mathbf{j}_K + \mathbf{j}_\nu = -\nu^{-1}\underbrace{\left(\frac{\nu M}{\mathcal{R}T}\underline{\underline{\mathcal{D}}}_K + \underline{\underline{K}}\right)}_{\underline{\underline{K}}_{app}}\nabla P \tag{12}$$

In gas mixtures, inter-species diffusion is an additional transport phenomenon. Binary diffusion coefficients can be expressed as :

$$\mathcal{D}_{ij} = \frac{1}{3}\left\langle c_{ij}\right\rangle\left\langle\lambda_{ij}\right\rangle \tag{13}$$

where the "ij" index refers to average quantities ~~made on~~relative to the $\{i, j\}$ gas species pair. In a porous medium, this expression is extended as:

$$\underline{\underline{\mathcal{D}}}_{ij} = \frac{\varepsilon}{3}\left\langle c_{ij}\right\rangle\left\langle\lambda_{ij}\right\rangle\underline{\underline{\eta}}_b^{-1} \tag{14}$$

where a third tortuosity tensor is defined. As stated before,~~Indeed,~~ there is no reason for the three tortuosity factors $\underline{\underline{\eta}}_b$, $\underline{\underline{\eta}}_K$ and $\underline{\underline{\eta}}_v$ to be equal to each other [28–30].

2.2. Regimes

Eq. (12) leads to a generalized Darcy relationship where an apparent permeability $\underline{\underline{K}}_{app}$ appears and is a function of the pore Knudsen number $Kn_p = \langle\lambda\rangle / \left\langle d_p \right\rangle$, as obtained by combining relations (5),(7), (9) and (11) :

$$\underline{\underline{K}}_{app} = \varepsilon \frac{\left\langle d_p \right\rangle^2}{32} \left[\underline{\underline{\eta}}_v^{-1} + \frac{256}{9\pi} \underline{\underline{\eta}}_K^{-1} Kn_p \right] \tag{15}$$

Assuming the tortuosities are of comparable magnitudes, this gives a critical Kn_p of ≈ 0.04. Indeed, four regimes are classically distinguished [31]:

- For very low $Kn_p < 0.01$, the regime is continuous,
- For $0.01 < Kn_p < 0.1$, the regime is called ”slip-flow”, also referred to as the Klinkenberg effect [32].
- For $0.1 < Kn_p < 10$, the regime is transitional,
- For Kn_p above 10, the regime is called ”free-molecular”.

Comparing eqs. (7) and (14), it is immediately seen that the contributions from Knudsen flow and from interspecies diffusion are equilibrated for a Kn_p number close to 1. So, it is of common practice to declare the $[0.02; 50]$ as a transition regime between a continuum regime and a free-molecule regime [33, 34].

The regimes and their limits are illustrated in Figure 1.

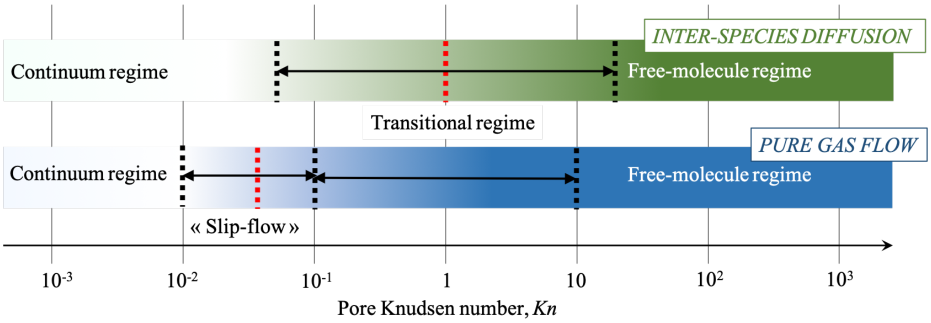

Figure 1: Different regimes according to the Knudsen number, for interspecies diffusion and for pure gas flow.

3. Models and correlations for gas transfer

3.1. *Models used for Chemical Vapor Infiltration*

Chemical vapor infiltration (CVI) is one of the most promising methods to manufacture ceramic-matrix composites without damaging the fibers used for reinforcement. Modelling of viscous flow and gas diffusion has been developed for many years on ideal simplified structures or on realistic 2D or 3D micrographs [18], some of them are described in this section and summarized in table 1. ~~Mostly,~~ Effective Knudsen diffusivities have been estimated for various porous media mostly using Monte Carlo Random Walk simulations. In 1989, Burganos and Sotirchos computed effective Knudsen diffusivities in 1D, 2D and 3D parallel random pore systems and randomly oriented pore systems for unimodal and bimodal pore size distributions [35]. The same year Sotirchos and Tomadakis [36] made the same kind of computations but in 1D, 2D, 3D bundles ~~structures~~ of parallel randomly overlapping fibers. In 1991, Tomadakis and Sotirchos presented effective Knudsen diffusion coefficients for 1D, 2D and 3D randomly overlapping fibers [37] and for 1D non-overlapping or partially overlapping fibers [38]. In order to facilitate the use of their diffusivity results, they developed, in their work for freely overlapping fibers [37], a three-parameter correlation that could ~~be used~~

~~to relate~~ connect the various tortuosity factors to the porosity of the medium :

$$\eta_j = \eta_{j,\mathrm{min}} \left(\frac{1-\varepsilon_p}{\varepsilon - \varepsilon_p} \right)^{\alpha_j} \qquad j = /\!/, \perp \tag{16}$$

ε_p is the percolation threshold and α_j a coefficient that depends on the fiber structure, the transfer type (binary diffusion or Knudsen diffusion) and on the diffusion direction.

For 1D non-overlapping fibers this expression became Eq. (17) that was used later for 2D and 3D structures.

$$\eta_j = \eta_j^{\mathrm{lim}} \left(\frac{\varepsilon_0-\varepsilon_p}{\varepsilon - \varepsilon_p} \right)^{\alpha_j} \qquad j = \perp, /\!/ \tag{17}$$

Here, ε_0 is the initial porosity and η_j^{lim} is the lowest possible tortuosity, obtained at the initial porosity. For porosities higher than 0.18 they found : $\eta_K = 1.747 \exp\left[1.4(1-\varepsilon)\right]$. Actually, eqs. (16) and (17) are extensions of Archie's law [39].

Many times effective Knudsen diffusivity has been compared with the effective diffusivity based on the mean pore diameter $\left\langle d_p \right\rangle = \frac{4\varepsilon}{S}$ using eq. (7) [35, 37]. Monte Carlo Random Walk simulations have been used for either Knudsen regimes or binary and transition regimes on ideal simplified media [33, 34, 40–42]. Melkote and Jensen used Monte Carlo Random Walk~~er~~ simulations on a 3D arrangement of fully penetrable cylinders to calculate ~~all regime~~ tortuosities in all regimes [40]. Ordinary diffusion tortuosities were found approximately equal to the reciprocal of the porosity (except for the lowest porosities), while the transition regime tortuosities are shown to deviate from the reciprocal porosity with a simple dependence on the Knudsen number. They finally compared Knudsen tortuosities with eq. (7). Tomadakis and Sotirchos made the same calculations on 1D, 2D and 3D cylindrical random capillaries structures [33] or random fiber structures [34]. Calculated transition tortuosities are compared to the Bosanquet relationship :

$$\underline{\underline{\eta}} = \frac{\underline{\underline{\eta}}_b + \underline{\underline{\eta}}_K Kn_p}{1 + Kn_p} \tag{18}$$

This equation was considered valid except for flow parallel to 1D structures. Binary regime tortuosity can also be calculated using eq.(17) [34]. Transvalidou simplified eq.(18) for ordered square arrays as:

$$\underline{\underline{\eta}} = \frac{\underline{\underline{\eta}}_b}{1 + Kn_p} \tag{19}$$

Permeability estimates have been assessed for a node-bond equivalent pore network [43] where porosity is made of spherical nodes, representing large pores at tow crossing points, connected by bonds (smaller channels ~~that connect~~between nodes). In this case the permeability coefficient depends on several specific parameters defining the node-bond network that are difficult to assess experimentally.

More recently a method derived from electrical conduction principles [27] has been tested and validated to predict permeability from the knowledge of effective bulk diffusivity for a variety of fibrous media [26, 44]. Using this principle for 1D, 2D and 3D randomly overlapping fibers and 1D non-overlapping fibers, Tomadakis and Robertson found the following relations for permeability coefficient, and viscous tortuosity :

$$K_j = \begin{cases} \dfrac{\left\langle d_f \right\rangle^2 \varepsilon}{32 \ln^2 \varepsilon} \dfrac{(\varepsilon - \varepsilon_p)^{\alpha_{b,j}+2}}{(1-\varepsilon_p)^{\alpha_{b,j}}[(\alpha_{b,j}+1)\varepsilon - \varepsilon_p]^2} & \text{for randomly overlapping fibers} \\ \dfrac{\left\langle d_f \right\rangle^2 \varepsilon^3}{32(1-\varepsilon)^2} \dfrac{e^{\alpha_{b,j}(\varepsilon-1)}}{(1+\alpha_{b,j}\varepsilon)^2} & \text{for 1D non-overlapping fibers} \end{cases} \quad j = //, \perp \tag{20}$$

This relation is translated in terms of tortuosities as:

$$\eta_{v,j} = \begin{cases} \eta_{b,j}\left(1 + \frac{\alpha_{b,j}\varepsilon}{\varepsilon-\varepsilon_p}\right)^2 & \text{for randomly overlapping fibers} \\ \eta_{b,j}\left(1 + \alpha_{b,j}\varepsilon\right)^2 & \text{for 1D non-overlapping fibers} \end{cases} \quad j = /\!/, \perp \tag{21}$$

Finally Skamser estimated permeability coefficients for 1D fibers bundles either from an ideal model or from 2D computed generated images [45]. For an initial porosity of 70%, a polynomial adjustment on a series of calculated points gives :

$$\frac{K_{/\!/}}{\left\langle d_f \right\rangle^2} = 2.24\varepsilon^2 + 0.0387\varepsilon \tag{22}$$

$$\frac{K_{\perp}}{\left\langle d_f \right\rangle^2} = 0.9110\varepsilon^2 - 0.379\varepsilon \text{ for } \varepsilon \in [0.4161; 0.7] \tag{23}$$

It is worth noting that eqs. (20),(22) and (23) are scaled with respect to the average (initial) fiber diameter instead of the average pore diameter as is done for diffusivities. The results for permeation perpendicular to the fiber direction are giving an unrealistically high percolation threshold (above 40%) - this is because they are obtained from computations based on 2D images, thereby missing the small gaps between fiber due to their actual 3D misaligment and waviness. Indeed, in complex realistic structures, 3D datasets obtained by X-ray CT [44, 46] should be used to compute diffusion or viscous flow.

At a larger scale, the Dusty-Gas Model [47] and the Binary Friction Model [48] are two models allowing a correct treatment of multicomponent diffusion in porous media, as soon as effective coefficients are provided for the three transfer modalities. In particular, this involves a good knowledge of the influence of the porous media structure on its morphological parameters, which are its porosity ε, its internal surface area S_v, its effective pore diameter $\left\langle d_p \right\rangle$ (usually related to the

Table 1: Several models for CVI

Ref.	Medium type	Studied parameters	Numerical methods	Equations	Porosity domain
Burganos & Sotirchos 1989 [35]	1D, 2D, 3D randomly overlapping cylindrical pores	Knudsen diffusion	MC/RW	$\underline{\underline{\mathcal{D}}}_K = \frac{1}{3}\varepsilon\underline{\underline{\mathcal{D}}}_K(\langle r_p\rangle)$	[0.3; 1]
Sotirchos & Tomadakis 1989 [36]	1D, 2D, 3D randomly overlapping capillaries	Knudsen diffusion	MC/RW	-	[0.3; 1]
Tomadakis & Sotirchos 1991a [37]	1D, 2D, 3D randomly overlapping fibers	Knudsen diffusion	MC/RW	Eq. (16)	[0; 1]
Tomadakis & Sotirchos 1991b [38]	1D non-overlapping and partially overlapping structures	Knudsen diffusion	MC/RW	Eq. (17)	[0; 1]
Melkote & Jensen 1992 [40]	3D fully Penetrable Cylinders (FPC)	Knudsen to continuum diffusion	MC/RW	$\eta - \frac{1}{\phi} = a + b\ln Kn_p + c(\ln Kn_p)^2$	[0.3; 0.6]
Tomadakis & Sotirchos 1993a [33]	1D, 2D, 3D cylindrical random capillaries	Knudsen to continuum diffusion	MC/RW	Eq. (18)	[0; 1]
Tomadakis & Sotirchos 1993b [34]	1D, 2D, 3D random fiber structures	Transition and continuum diffusion	MC/RW	Eq. (18) and Eq. (17) for η_b	[0; 1]
Transvalidou & Sotirchos 1996 [42]	1D square array of bundles	Knudsen to continuum diffusion	MC/RW	Eq. (18)	[0; 1]
Skamser 1994 [45]	1-D partially overlapping bundles of fibers + 2D micrographs	Viscous flow	”‘marker-and cell”’ Stokes eq. solver (FD)	Eqs. (22-23)	[0; 0.7]
Tomadakis & Robertson 2005 [26]	1D, 2D, 3D randomly overlapping cylindrical fibers and 1D non-overlapping random array of fibers	Viscous flow	MC/RW + electrical conduction principle	Eq. (21) and (20)	[0.2; 1]
Vignoles & Coindreau 2007 [44]	3D X-ray μ-CT scans of real fibrous media	Viscous flow and Knudsen to continuum diffusion	Finite Volumes and MC/RW	Eq. (17) and $\underline{\underline{\eta_v}} = \frac{\underline{\underline{\eta_b}}}{M}\left(1 + \frac{\alpha\varepsilon}{\varepsilon - \varepsilon_p}\right)^2$	[0; 1]

former two parameters by Eq.(46)), and its tortuosities $\underline{\underline{\eta}}_b$, $\underline{\underline{\eta}}_K$ and $\underline{\underline{\eta}}_v$. One of the issues at stake here is that, by infiltration, a large range of porosity (or SVF) is covered, starting from a fibrous preform – which can be considered as similar to a fibrous filter – to a poorly porous material in which the solid fraction cannot be described any more as an arrangement of fibers. In some way one has to switch between solid-related quantities to pore-related quantities.

It is therefore of interest to provide estimates of the average fiber diameter $\langle d_f\rangle$ as well as to the average pore diameter $\langle d_p\rangle$. Additionally, fibers are partially clustered, so that the diameter of the initial fibers, which is well known, is not the most pertinent geometrical indicator for mass transfer.

3.2. Models developed for fibrous filters

As opposed to the aforementioned relationships, it is usual in filters literature to use the fibers average radius $\left\langle r_f \right\rangle$ instead of the pore diameter [1]. There are numerous studies, starting from I. Langmuir in 1942 [49] who derived from the expression of the drag force past a single cylinder in a circular unit cell, when fibers are all parallel to the flow direction. He then extended his relation to non-ideal media introducing a geometrical factor B [50]:

$$K_{1D,/\!/} = \frac{\left\langle d_f \right\rangle^2}{16\phi B}\left(-\frac{3}{2} - \ln\phi + 2\phi - \frac{\phi^2}{2}\right) \tag{24}$$

where ϕ is the Solid Volume Fraction (SVF). This expression has been popularized by Happel [51] and has been extensively used later. More recently Drummond and Tahir [52] used a method by matching a solution outside one cylinder to a sum of solutions with equal singularities inside every cylinder to find the flow field in square, triangular, hexagonal and rectangular array with the following formula:

$$K_{1D,/\!/} = \frac{\left\langle d_f \right\rangle^2}{16\phi}\left(-\ln\phi + \kappa + 2\phi - \frac{\phi^2}{2}\right) \tag{25}$$

where κ depends on array geometry.

More recently, Tamayol [53] investigated analytically flow parallel to ordered fibers structures considering square, and hexagonal close packing arrays of cylinders.

$$K_{1D,/\!/} = \begin{cases} \frac{\langle d_f \rangle^2}{16\phi}\left(-1.479 - \ln\phi + 2\phi + \frac{\phi^2}{2} - 0.0186\phi^4\right): & \text{square array} \\ \frac{\langle d_f \rangle^2}{16\phi}\left(-1.352 - \ln\phi + 2\phi + \frac{\phi^2}{2} - 0.246\phi^6\right): & \text{hexagonal array} \end{cases} \tag{26}$$

---

[1] Throughout this document we will only use fiber *diameters* instead of radii.

Happel [51] also found an equation for flow perpendicular to arrays of cylinders :

$$K_{1D,\perp} = \frac{\left\langle d_f \right\rangle^2}{16\phi}\left(-\frac{1}{2}\ln\phi + \frac{\phi^2 - 1}{\phi^2 + 1}\right) \tag{27}$$

The same year, Kuwabara [54] used the same model as Happel but with a vorticity-free boundary condition and derived the following expression :

$$K_{1D,\perp} = \frac{\left\langle d_f \right\rangle^2}{16\phi}\left(-\frac{1}{2}\ln\phi - \frac{3}{4} + \phi + \frac{\phi^2}{4}\right) \tag{28}$$

The factor between parentheses is called the Kuwabara factor Ku.

Many authors proposed others expressions, including Davies [55] who presented an empirical correlation which fit experimental data :

$$K_{1D,\perp} = \frac{\left\langle d_f \right\rangle^2}{16\phi^{3/2}}\left(1 + 56\phi^3\right)^{-1} \tag{29}$$

~~Then, i~~In the same way Tamayol also investigated perpendicular flow to 1D, 2D and 3D structures [56] and found that the fiber arrangement plays an important role for $\varepsilon < 0.7$:

$$K_{1D,\perp} = \begin{cases} \dfrac{0.16\left\langle d_f \right\rangle^2\left[\frac{\pi}{4\phi} - 3\sqrt{\frac{\pi}{4\phi}} + 3 - \sqrt{\frac{4\phi}{\pi}}\right]}{\sqrt{1-\phi}} : & \text{square array} \\ \dfrac{0.16\left\langle d_f \right\rangle^2\left[\frac{\pi}{3\sqrt{3}\phi} - 3\sqrt{\frac{\pi}{3\sqrt{3}\phi}} + 3 - \sqrt{\frac{3\sqrt{3}\phi}{\pi}}\right]}{\sqrt{1-\phi}} : & \text{hexagonal array} \end{cases} \tag{30}$$

$$K_{2D,\perp} = 0.008\left\langle d_f \right\rangle^2 \sqrt{1-\phi}\left[\left(\frac{\pi}{4\phi}\right)^2 - \frac{2\pi}{4\phi} + 1\right] \tag{31}$$

$$K_{3D} = 0.08\frac{(S - \left\langle d_f \right\rangle)^4}{S^2(1-\phi)^{0.3}} \tag{32}$$

Most of these models display a limited range of validity; they are mostly adequate for low SVF values.

3.3. Other models for Darcian permeability of fibrous media

It is impossible here to make an exhaustive list of all models proposed by tens of contributors in the past 80 years; however we have selected some of them for sake of comparison to the results presented later in this paper.

Considering 1D fibers media Van der Westhuizen [57] used the phase average Navier Stokes equation to estimate parallel and transverse permeability of random unidirectional fiber bed :

$$K_{1D,/\!/} = \frac{\left\langle d_f \right\rangle^2}{16\phi} \frac{\pi}{6} (1-\phi) \left(\phi^{-1/2} + \phi^{1/2} - 2\right) \tag{33}$$

$$K_{1D,\perp} = \frac{\left\langle d_f \right\rangle^2}{16\phi} \frac{(3.142 + 2.157\,\phi)\,(1-\phi)^2}{12} \tag{34}$$

Sangani and Acrivos [58] used a least-squares technique to solve the problem of normal flow through square and hexagonal arrays. At high SVF their results are asymptotic to lubrication theory, and at low SVF their results are asymptotic to an analytical solution which they developed (Eq. (35)) :

$$K_{1D,\perp} = \begin{cases} \frac{\langle d_f \rangle^2}{16\phi} \left(-\frac{\ln\phi}{2} - 0.738 + \phi - 0.887\phi^2 + 2.038\phi^3 + O(\phi^4)\right) : & \text{square array} \\ \frac{\langle d_f \rangle^2}{16\phi} \left(-\frac{\ln\phi}{2} - 0.745 + \phi - \frac{\phi^2}{4} + O(\phi^4)\right) : & \text{hexagonal array} \end{cases} \tag{35}$$

Considering fiber mats, many models can be extracted from literature data. Van Doormaal and Pharoah [59] calculated through-plane and in-plane permeability using a Lattice Boltzmann Method for different fiber arrangements in which the angle between fibers in neighboring layers is a value between 0 and 90°. They found the following relations for $0.6 \leq \varepsilon \leq 0.8$:

$$K_{2D,\perp} = \frac{\left\langle d_f \right\rangle^2}{16\phi} 1.12 \left(1 - \phi\right)^{4.3} \tag{36}$$

$$K_{2D,\perp} = \frac{\left\langle d_f \right\rangle^2}{16\phi} 1.04 \left(1 - \phi\right)^{3.6} \tag{37}$$

Clague *et al.* [60] have studied permeability by numerical simulations (Lattice Boltzmann method) on 2D square arrays of cylinders and found good correlations with the results of Sangani and Acrivos [58] ~~result~~s.

In the transverse direction to the fiber mats, Shou [61] carried out a theoretical study on the permeability of 1D, 2D and 3D fibrous media with high porosity ($0.7 < \varepsilon < 1$).

Soltani [62] reconstructed 3D images of 2D needled fibers structures in order to calculate in-plane and through-plane permeabilities by fluid flow simulations and compared the results with experimental data for $0.7 < \varepsilon < 1$.

In addition to all of these models numerous experimental permeability values were retrieved from the publications of Kostornov [63] who worked on water and alcohol flows through 2D metal fibers. Some values were also extracted from the publications of Gauvin [64] (five randomly arranged fiber mats), Shih [65] (fiberglass mats) and Young [66] (fiber mats for resin injection molding process).

To summarize these works, Table 2 collects all models given either in fiber-related quantities or in pore-related quantities.

3.4. Gas transfer in slip-flow and rarefied regime in filters

The effect of gas rarefaction has been considered first in the study of air filters, starting with ~~studies~~works performed by Pich [67] and Glushkov [68] in the free-

Table 2: Several models for Darcian permeabilities of fibrous media

Ref.	Medium type	Reduced permeability	Validity domain
Flow perpendicular to fibers			
Kuwabara 1959 [54]	Parallel cylinders	Eq. (28)	$\phi \in [0; 0.1]$
Happel 1959 [51]	Parallel cylinders	Eq. (27)	$\phi \in [0; 0.5]$
Davies 1953 [55]	Parallel cylinders	Eq. (29)	$\phi \in [0.006; 0.3]$
Van der Westhuizen 1996 [57]	Parallel cylinders	Eq. (34)	$\phi \in [0; 0.8]$
Tamayol 2011 [56]	1D, 2D and 3D arrays of cylinders	Eq. (30),(31)and (32)	$\phi \in [0; 0.5]$
Van Doormaal & Pharoah [59]	2D fiber mats	Eq. (36)	$\phi \in [0.2; 0.4]$
Sangani & Acrivos 1982 [58]	1D arrays of cylinders	Eq. (35)	$\phi \ll 1$
Flow parallel to fibers			
Langmuir 1942 [49]	Parallel cylinders	Eq. (24)	$\phi \in [0; 0.1]$
Happel 1959 [51]	Parallel cylinders	Eq. (24)	$\phi \in [0; 0.5]$
Drummond & Tahir 1984 [52]	1D arrays of cylinders	Eq. (25)	$\phi \in [0; 0.35]$
Tamayol 2010 [53]	1D arrays of cylinders	Eq. (26)	$\phi \in [0; 0.6]$
Van der Westhuizen 1996 [57]	Parallel cylinders	Eq. (33)	$\phi \in [0; 0.8]$
Van Doormaal & Pharoah [59]	2D fiber mats	Eq. (37)	$\phi \in [0.2; 0.4]$

molecule regime. Introducing a fiber-related Knudsen number $Kn_f = \frac{\langle \lambda \rangle}{\langle d_f \rangle}$, their correlations can be written as :

$$K_{\mathrm{eff}_\perp} \approx \frac{\left\langle d_f \right\rangle^2}{16\phi} \frac{64}{3\pi C} Kn_f \tag{38}$$

where C is a constant (2.67 for Glushkov, 2.91 for Pich). Here we recognize that the effective permeability increases as an affine function of the Knudsen number, as in Eq. (15).

When studying the slip-flow regime (*i.e.* for $0.001 \leq Kn_f \leq 0.1$) Pich [67] obtained the following expression :

$$K_{\mathrm{eff}_\perp} = \frac{\left\langle d_f \right\rangle^2}{16\phi} \frac{Ku + 1.996 Kn_f \left(-\frac{1}{2} - \ln\phi + \frac{\phi^2}{2} \right)}{1 + 3.992 Kn_f} \tag{39}$$

Yeh and Liu [69] have obtained the following relationship, which is quite similar in behavior:

$$K_{\mathrm{eff}_{\perp}} \approx \frac{\left\langle d_f \right\rangle^2}{16\phi} \left(-\frac{1}{2} \ln \phi - \frac{\phi^2}{4} + \frac{-\frac{3}{4} + \phi + Kn_f \frac{(2\phi-1)^2}{2}}{1 + 2Kn_f} \right) \tag{40}$$

These two relations give a finite asymptotic value of the permeability in the free-molecule regime ($Kn_f \rightarrow \infty$), instead of a linear dependence to the Knudsen number, which is not expected to be correct.

Pich, for dilute fibers and low Knudsen numbers, also proposed the following approximation [70]:

$$K_{\mathrm{eff}_{\perp}} \approx \frac{\left\langle d_f \right\rangle^2}{16\phi} \left(-\frac{3}{4} - \frac{1}{2} \ln \phi + 1.996 Kn_f \right) \tag{41}$$

This model seems more adequate for the whole range of Knudsen numbers.

Rather similarly, Kirsch [4] proposed on a semi-empirical basis the following law :

$$K_{\mathrm{eff}_{\perp}} = K_0 + \frac{\left\langle d_f \right\rangle^2}{16\phi} 1.43 \left(1 - \phi\right) \eta_v'^{1/2} Kn_f \tag{42}$$

where the ”inhomogeneity factor” $\eta_v' = K_{\mathrm{ref}}/K_0$ is the ratio between the reference permeability at $Kn = 0$ in the case of an ideal arrangement of equally spaced identical parallel fibers [4] and the actually measured value K_0 (for parallel fibers $\eta_v' = 1$. Instead of the Langmuir-Happel-Kuwabara expression he chose for K_{ref} :

$$K_{\mathrm{ref}_{\perp}} = \frac{\left\langle d_f \right\rangle^2}{16\phi} \left(-0.5 \ln \phi - 0.52 + 0.64\phi\right)^{-1} \tag{43}$$

Relation (42) has been recently verified on nano-fiber filters with larger values of the ”inhomogeneity coefficient” [71]. This relation is so far the only attempt to try and correlate the dimensionless geometrical hindrance factor (here “inhomogeneity factor”, or “tortuosity”, as used in other literature) linked to viscous flow to the one of free-molecule flow.

The different models from literature lead to the following general formulation :

$$K_{\text{app}} \approx K + \frac{\left\langle d_f \right\rangle^2}{16\phi} \tau \cdot Kn_f \tag{44}$$

where τ is a factor differing from author to author. Table 3 summarizes these expressions.

Table 3: Expressions of coefficient τ in literature for flow perpendicular to beds of circular fibers.

Reference	Regime	τ
Pich [70]	$Kn \to \infty$	2.336
Glushkov [68]	$Kn \to \infty$	2.544
Pich [70]	$Kn \leq 0.01$	$1.996\,(1 - 2\phi)$
Yeh and Liu [69]	$Kn \leq 0.01$	$2\left(1 - 2\phi + \frac{\phi^2}{2}\right)$
Kirsch [4]	-	$1.424\varepsilon\eta_v'^{1/2}$

3.5. *From solid-related to pore-related indicators*

One difficulty with viscous flow through porous media is that the physically significant length scale is a pore diameter, whereas what is often available experimentally in fibrous media is the fiber diameter. A crucial issue is therefore to obtain a sound relationship between these two quantities. In order to obtain a general correlation, useful for many types of porous media, Kozeny and Carman [72] developed an expression where the primarily involved quantity is the internal surface area S_v:

$$K = \frac{\varepsilon^3}{k_{KC} S_v^2} \tag{45}$$

where the constant k_{KC} depends on the family of investigated porous media and on the orientation. The internal surface area is related to the specific surface area of the fibers S_s (m^2 of surface per m^3 of solid volume) in a porous filter through multiplication by the SVF : $S_v = \phi S_s$. It is useful to recall that the internal surface area can be related either to the fiber diameter or to the hydraulic pore diameter [73]:

$$S_v = \frac{4\phi}{\langle d_f \rangle} = \frac{4\varepsilon}{\langle d_p \rangle} \tag{46}$$

Accordingly, two expressions can be derived from the Kozeny-Carman relation, one with solid-related quantities:

$$K = \frac{(1-\phi)^3}{\phi^2} \frac{\langle d_f \rangle^2}{16 k_{KC}} \tag{47}$$

and one with pore-related quantities:

$$K = \varepsilon \frac{\langle d_p \rangle^2}{16 k_{KC}} \tag{48}$$

in which we recognize that the tortuosity is half of the Kozeny constant.

In this approach, the determination of the Kozeny constant is the most controversial issue because it is mainly influenced by the geometric characteristics of porous media, which are hard to define. A number of studies have investigated the relationship between Kozeny constant and porosity, fiber diameter or tortuosity [74–79].

To conclude this section, there are many models in the literature which deal with ~~the~~ gas transport in fibrous media especially for filters media. In contrast there is few experimental data on permeability, especially for the CVI process. ~~Most of the time~~In most occurrences gas transport is related to fiber diameter whereas it is the pore diameter which drives physical phenomena. That does not provide an experimental basis to link fiber and pore-related properties.

4. Experimental

4.1. Description of materials

Partly infiltrated C_f/C composites were studied. All these materials are obtained from a preform made of carbon yarn sheets (Fig. 2,a), horizontally stacked by winding ($x - y$ plane) (Fig. 2,b). Then, these layers are needle-punched in the transverse direction (z) to hold stacks together (Fig. 2,c). As a consequence, some yarns are broken and partially transferred in the z direction [80].

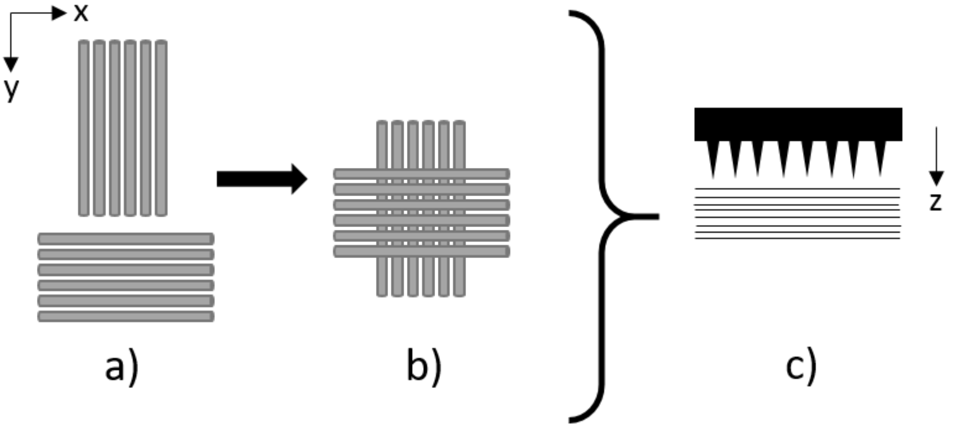

Figure 2: Carbon fibrous preform manufacturing

A yarn is less than 1 mm in diameter size and contains a large number of fibers around 7 µm of diameter. There are three scales of porosity to consider in order to correctly assess the properties of the preform : (*i*) pores inside a yarn (micropores), (*ii*) pores between yarns (mesopores), and (*iii*) pores between layers (macropores)(Fig. 3). The words ”micro-”, ”meso-” and ”macro-pores” should not be understood in the IUPAC sense, but only refer to the *ad hoc* definitions of micro-, meso- and macro-scales pertinent in this study.

In order to observe the structural changes of these fibrous media during the CVI process, different cylindrical samples were extracted from the preform at different stages of infiltration. Skeletal density was measured by a Micromeritics

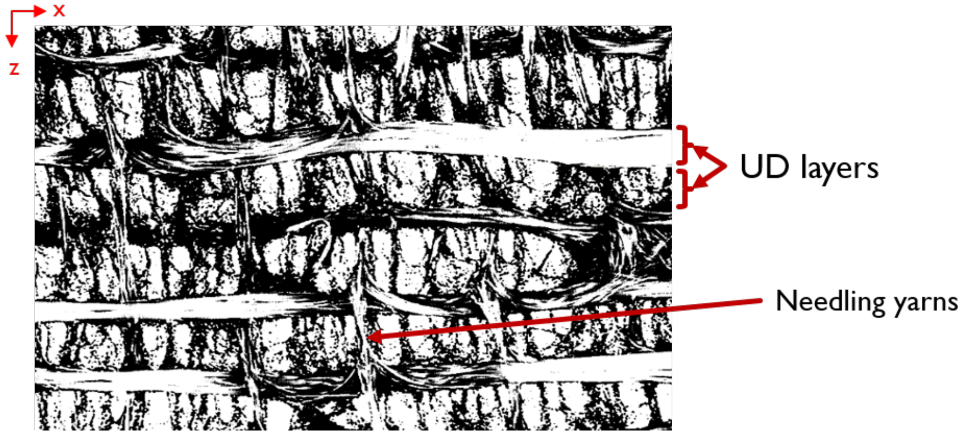

Figure 3: Rendering of a C_f/C composite microstructure and porosity on X-Ray Computerized Tomographic scan

AccuPyc 1340-10 helium pycnometer in order to calculate the porosity of the samples. Specific surface area was obtained by nitrogen adsorption at 77 K in a Micromeritics ASAP 2010 apparatus according to the BET method [81] and pore size distribution by a Micromeritics Autopore IV mercury porosimeter.

4.2. Tomography and image analysis

X-Ray micro Computerized Tomography (µCT) images of the whole samples were acquired on a GE (formerly Phoenix) v|tome|x µCT scanner. The apparatus was operated with a voltage of 100 kV and an intensity of 240 µA using a 180 kV tube, a micro focus beam in mode 0 and a filter of 0.1 mm of copper. The samples were positioned at 37.5 mm from the X-Ray source to obtain a pixel size of 8 µm. For each scan, 2,500 2D radiographs were recorded on 360° using an exposure time of 1 s and averaging on 2 images. A region of interest (ROI) of approximately $1200 \times 1200 \times 1400$ voxels was selected on the CT images (corresponding to $9.6 \times 9.6 \times 11.2$ mm^3). Figure 4 shows images obtained from samples at different infiltration stages. At such a resolution, it is difficult to distinguish the fibres from the matrix, due to their barely distinct densities. In contrast we can easily observe the pore space.

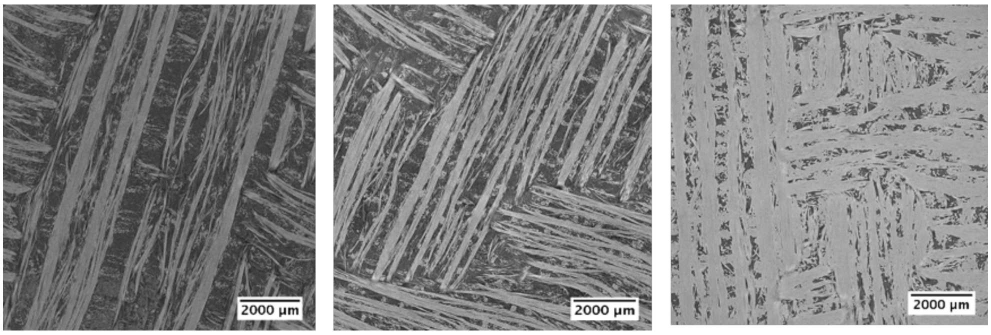

Figure 4: X-ray μ-CT scans (8 µm/pix) of carbon/carbon composites with different densities (from left to right, the average density is equal to 0.85, 1.04 and 1.71 g.cm^{-3})

For a better differenciation of the two phases, an image binarization step is necessary. Thresholding is one of the simplest and fastest segmentation methods. The objective is to set a threshold above which greyscale levels represent the solid and below which greyscale levels correspond to the pore space. In our case, the greyscale level histogram of each sample shows two peaks that correspond to the two phases and a valley representing an uncertain zone where the threshold must be chosen (Fig. 5).

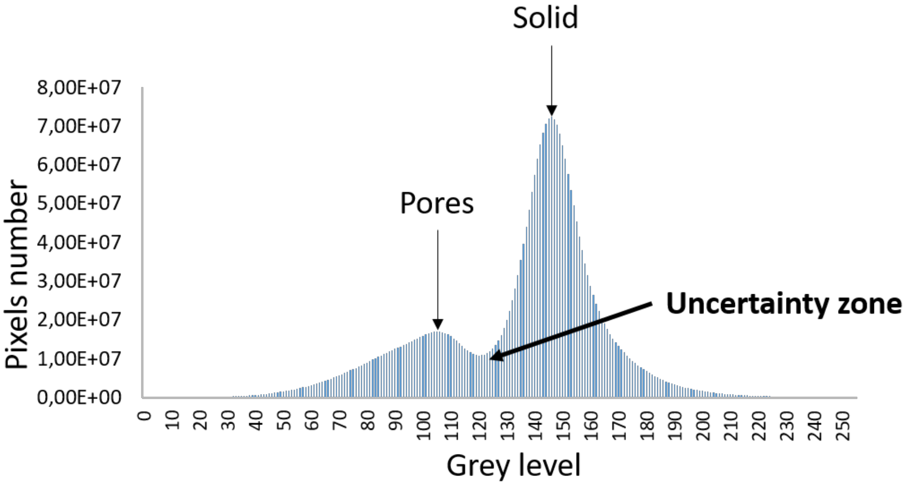

Figure 5: Greyscale levels histogram of a C/C composite

The Ōtsu thresholding method has been chosen to obtain binary images from the CT scans. This technique seeks to minimize the intra-class variance [82], defined as a weighted sum of the two classes corresponding to the two different phases.

Figure 6 shows an image of a sample before and after binarization.

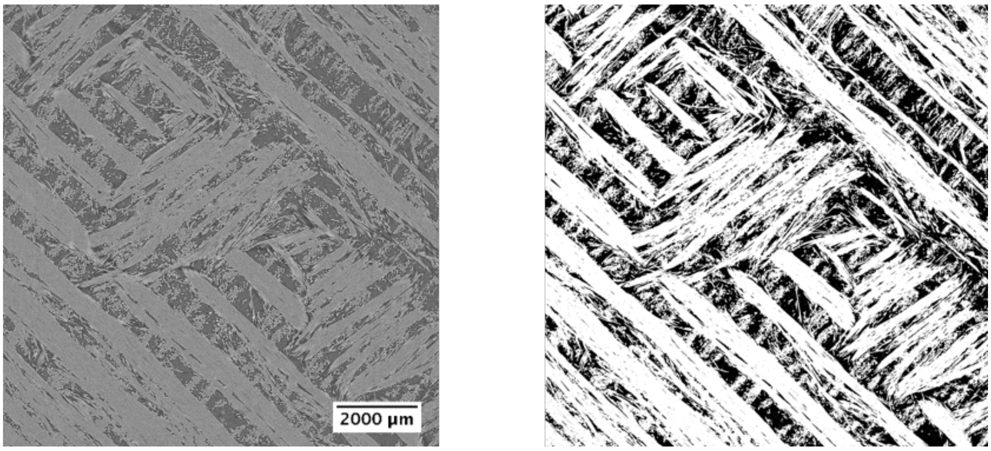

Figure 6: X-ray CT scans images before (left) and after (right) segmentation

In addition to porosity, other geometrical quantities of interest have been evaluated : (*i*) the internal surface area, for which the Simplified Marching Cube (SMC) discretization scheme has been used [83] and (*ii*) the average chord lengths, obtained by drawing random segments between surfaces obtained by SMC. Previous calculations had shown consistent results on an ideal cylindrical pore [41].

In order to compare the results to another kind of material with different microstructures, 3D μ-CT scans were performed on two Calcarb ® CBCF 15-2000 materials [84]. These materials are made of carbon fiber felts, barely consolidated with pyrolyzed phenolic resin traces. The porosity of these materials is around 91 percent. In order to have a variety of porosity values, the images were numerically infiltrated with the MC/RW code described later [85]. Snapshots of the resulting media are provided in Fig. 7.

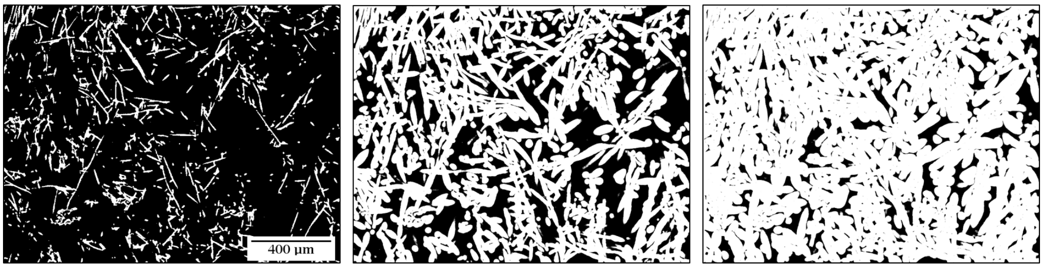

Figure 7: X-ray μ-CT scans (2 µm/pix) of Calcarb ® CBCF 15-2000 composites with different porosities (from left to right, the porosity is equal to 0.91, 0.49 and 0.21)

4.3. Experimental set-up for gas flow through porous media

An experimental low-pressure gas permeation set-up (from 5 to 30 kPa) was used to measure the composites permeability and Knudsen diffusivity coefficients (Fig. 8). No attempt has been made to measure the interspecies diffusion; only pure nitrogen has been used as a working gas. Experiments have been run at ambient temperature; indeed, it has been shown that high-temperature measurements give the same results on permeability and Klinkenberg corrections [7].

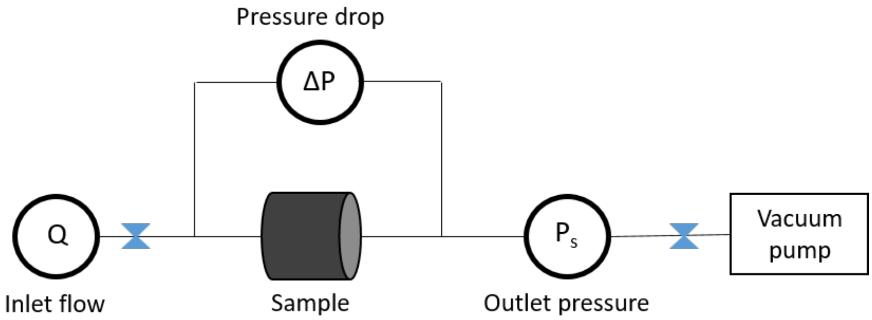

Figure 8: Permeametry experimental set-up

The samples are inserted in a measurement cell (diameter A, length L), ensuring they are correctly fitted without compression. We have not characterized the raw preforms, upon finding that they were not mechanically strong enough to resist insertion in the measurement cell. The most porous samples we have characterized are already slightly consolidated by a small amount of infiltrated matrix.

The measurement principle is to send nitrogen to the sample inlet; the gas flows through the sample by applying a lower pressure at the other side, using a vacuum pump. The output pressure is regulated by a pressure gauge (Baratron 626B) and a driven throttle valve. A pressure drop detector (MKS PR4000) is connected in derivation with respect to the cell holding material. Measurements are carried out in steady-state conditions, since the transient times are short for this type of medium with permeabilities around 1 Darcy. The output pressure P_{out} and the inlet mass flow rate Q are varied and the corresponding pressure drop values ΔP are recorded after the transient pressure variations have faded away. By rewriting and using the equation (12) and considering 1D gas transfer, one has:

$$\frac{Q}{\Delta P} = \left[\frac{K}{\mu} \underbrace{\left(P_{out} + \frac{\Delta P}{2} \right)}_{P_{av}} + \mathcal{D}_K \right] \frac{A}{L} \frac{M}{\mathcal{R}T} \tag{49}$$

Plotting $Q/\Delta P$ as a function of the average pressure P_{av} gives a straight line where the Knudsen diffusivity coefficient $\mathcal{D}_K$ can be determined by the ordinate at the origin b and the permeability K by the slope a.

$$b = \mathcal{D}_K \frac{A}{L} \frac{M}{\mathcal{R}T} \tag{50}$$

$$a = \frac{K}{\mu} \frac{A}{L} \frac{M}{\mathcal{R}T} \tag{51}$$

As shown in the example of figure 9, the linear relationship is well verified.

4.4. Numerical methods

All computations have been carried out using the X-ray μ-CT scans as resolution domains. On the one hand, gas diffusion (binary and Knudsen) numerical

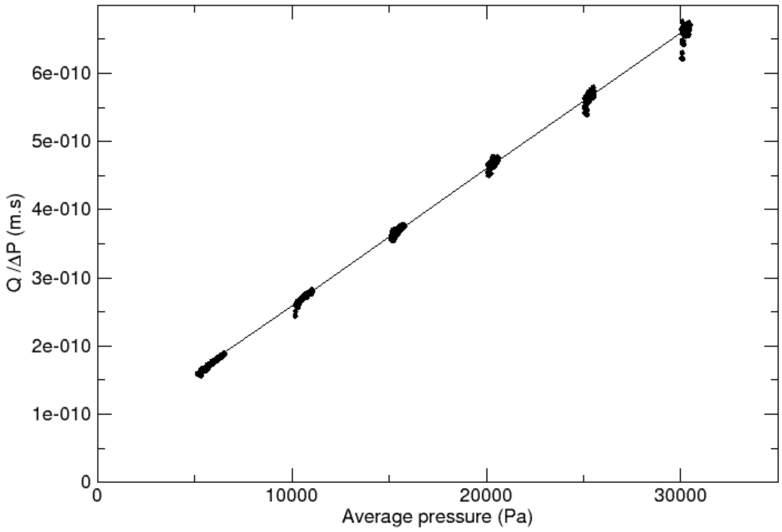

Figure 9: An example of experimental results: plot of $Q/\Delta P$ *vs.* P_{av} and fit of Eq. (49).

experiments have been conducted by the Monte/Carlo Random Walk technique [15, 36, 40, 41]. On the other hand, direct viscous permeability computations have been made with a home-made Finite Volume solver. Details on these numerical methods are provided below.

4.4.1. Monte-Carlo Random Walks for binary and Knudsen diffusion

Numerical gas diffusion simulations were run for each sample using a computer code developed earlier [41]. This code firstly discretizes the fluid/solid interface following the Simplified Marching Cube (SMC) scheme [83]. Then, a sufficient number of random walkers is randomly introduced in the fluid phase of the images (here, $N_w = 10000$ walkers). These walkers move in random directions until they reach the end of their free path λ (which simulates a molecule-molecule collision) or a wall; they then change their direction according to a random sampling with isotropic distribution (after a molecule-molecule collision) or with Knudsen's cosine law (after a molecule-wall collision) and a new free path is sampled randomly with a decreasing exponential distribution with average $\langle \lambda \rangle$. This requires probing the presence of pore walls at each cell, which is conveniently carried out thanks to the SMC scheme. The algorithm is sketched at Fig. 10. Obtaining an average effective diffusion coefficient requires having the random walkers to travel for a sufficiently long time in the initial image or in its repetitions over space. Accordingly, when a random walkers hit an image boundary, it is allowed to re-enter the image by the opposed boundary. Two sets of coordinates (and direction vectors) have to be followed separately : local coordinates of the molecule inside the loaded image, and global coordinates, which are used for the computation of the total displacements. Various possibilities are to determine the local coordinates after crossing a boundary : (*i*) reflection (symmetry), (*ii*) reentrance by the opposite face (translation), (*iii*) random reintroduction in the void space (random translation), (*iv*) reentrance at a random location of the void part of the opposite face. Condition (*iv*) is particularly well suited to the type of image treated here, at it allows an unbiased identification of the eigenvectors of the diffusivity tensor [86].

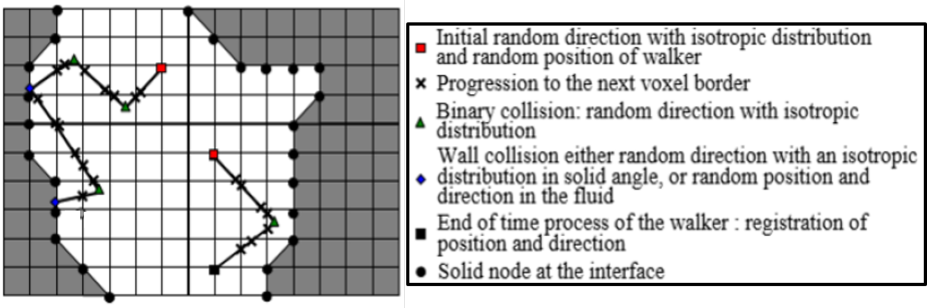

Figure 10: Random walkers displacements in 2D example

The computed effective diffusion coefficients are then obtained by using the

Einstein relationship [15, 87–90]:

$$\underline{\underline{\mathcal{D}}}^{\mathrm{eff}} = \lim_{\substack{t\to\infty \\ N_w\to\infty}} \frac{\operatorname{cov}(\xi,\xi)}{2t}, \tag{52}$$

where ξ is the displacement vector of a walker from the initial position during its travel time t.

Depending on the Kn number, the effective diffusion coefficient tends to a binary diffusion limit for low Kn and towards a Knudsen diffusion limit at high Kn. The Bosanquet relationship (18) is in general well verified.

The results obtained in the continuum regime will also be utilized to calculate permeability coefficients using the technique suggested by Tomadakis & Robertson [26] explained in the results section.

4.4.2. Finite Volumes for viscous flow

The values of the permeabilities are obtained from micro-scale images by a Stokes-Darcy change of scale. At low Reynolds numbers, it is sufficient to describe the fluid movement by the continuity and Stokes equations in the fluid domain Ω_f, subjected to the adherence boundary condition at the fluid -solid interface $\partial\Omega_{fs}$:

$$\left\{\begin{array}{rcll} \nabla\cdot\mathbf{u} & = & 0 & \text{in} \quad \Omega_f \\ -\mu\nabla^2\mathbf{u} & = & \nabla P & \text{in} \quad \Omega_f \\ \mathbf{u} & = & 0 & \text{at} \quad \partial\Omega_{fs} \end{array}\right. \tag{53}$$

Either by homogenization [91, 92] or by volume averaging [93], the macroscopic behaviour is proved to obey Darcy's law [94]. The numerical values of the permeability tensor coefficients may be attained performing three numerical experiments, in which the macroscopic pressure gradient $\nabla\langle P\rangle$ is assigned respectively to $G_x\mathbf{e}_x$, $G_y\mathbf{e}_y$ and $G_z\mathbf{e}_z$, *ie.* along the three principal directions, whereas the velocity is subjected to null-gradient boundary conditions at the image edges. The lines of the permeability tensor are then obtained from the computed velocity field $\mathbf{u}(\mathbf{r})$ in each test:

$$K_{i,j} = -\mu \langle u_i \rangle G_j^{-1} \tag{54}$$

The PeSto (Permeability Stokes) code is used to solve these problems, using a Finite Volume discretization scheme. An inherent difficulty in solving the Stokes equations is the decoupling between pressure and velocity, added to the fact that pressure does not explicitly appear in the continuity equation. One of the first techniques to overcome this difficulty was proposed by Chorin [95] : the introduction of an an artificial compressibility. The continuity equation is replaced by the following unsteady one:

$$\beta^{-1} \frac{\partial P}{\partial t} + \nabla \cdot \mathbf{u} = 0 \tag{55}$$

where β is a numerical parameter to be adjusted in order to ensure the mass conservation constraint. A high value of the parameter β will make it possible to restore the incompressible behaviour to the detriment of the numerical scheme stability. In PeSto the equations for the momentum conservation are solved by integration in finite volumes ; the mesh is directly constructed from a conversion of the porous part of the tomographic images : each voxel corresponds to a cubic control volume, leading to a completely structured mesh. The discretized momentum conservation equations lead to a linear system to be solved at each time step. The sparse matrix system is initially assembled in a sparse “coordinates” format, and then converted to a “Compressed Sparse Rows” format. The system is solved with a biconjugate gradient stabilized method (BiCGStab) [96], preconditioned with the ILU(0) method (Incomplete Lower-Upper decomposition with zero fill-In) [97].

These calculations take a long time to converge, especially for very porous

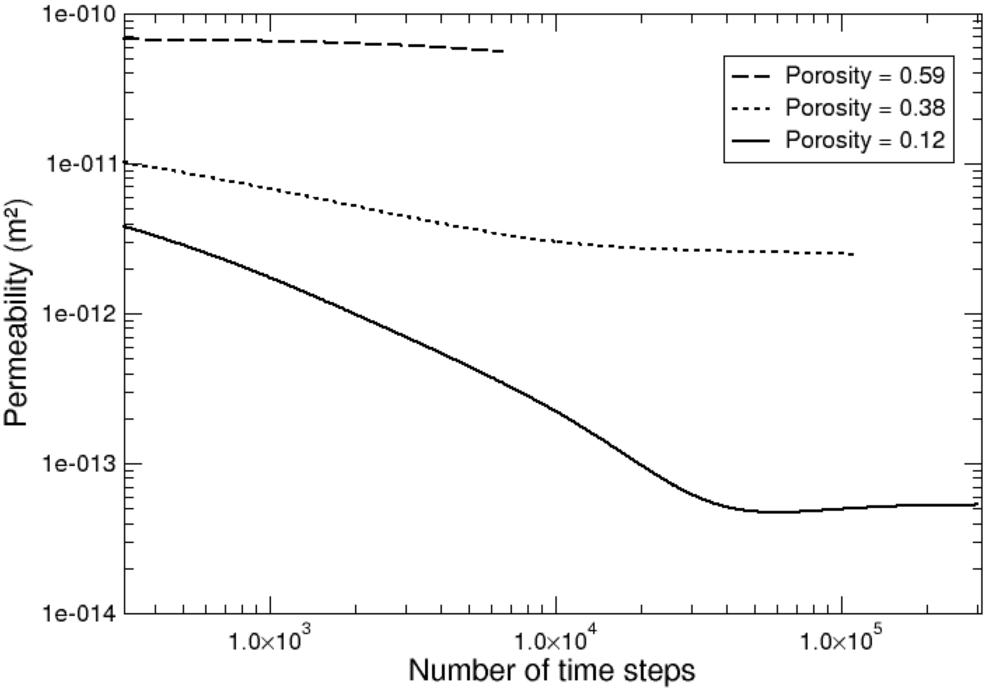

Figure 11: Convergence of permeability coefficients after two weeks of computation by PeSto code for materials with different porosities

materials. Figure 11 represents the calculated permeability coefficients after two weeks of computation for materials with different porosities. Because of that, calculations were performed on a small number of samples.

5. Results

In this section, we will first check the level of accuracy of the image processing techniques with respect to experimental data, and discuss the relation between porosity, internal surface area, average pore diameter and average "fiber" diameter. Then, a confrontation of the experimental results to the image-based simulations will be carried out for free-molecule flow and for viscous flow.

5.1. Geometrical and morphological indicators

Because all the simulations are performed on X-ray μ-CT scans, it is important to calculate numerical porosity, internal surface area, pore diameter and mean chord length in solid or void phases, and to compare the results with experimental data and analytical results from model fiber structures.

5.1.1. Porosity

Numerical porosity can easily be determined from CT scans, in which the solid phase is separated from the fluid one, by calculating the ratio between the number of fluid phase voxels and the total number of voxels. The numerical porosity evolution with density is compared with the porosity measured by helium pycnometry and to a theoretical porosity calculated from constituent densities :

$$\rho_{material} = \rho_{fibers} * \phi_{fibers} + \rho_{matrix} * \phi_{matrix} \qquad (56)$$

With :

$$\phi_{matrix} = 1 - \varepsilon - \phi_{fibers} \qquad (57)$$

The uncertainty of the experimental values is very low (around 1%), and that of numerical values is about 5%. The results between theoretical and experimental values are very close, but the difference with the numerical values is not negligible. Numerical porosities appear to be slightly overestimated : that may come from a loss of information after the pore/solid interface discretization or from tomographic image resolution which is not high enough to provide accurate results.

5.1.2. Surface area

Numerical internal surface area of the materials is in the same way compared to experimental results obtained from nitrogen adsorption BET measurements for ~~all~~the whole material porosity range. The results are shown in Fig. 13. The

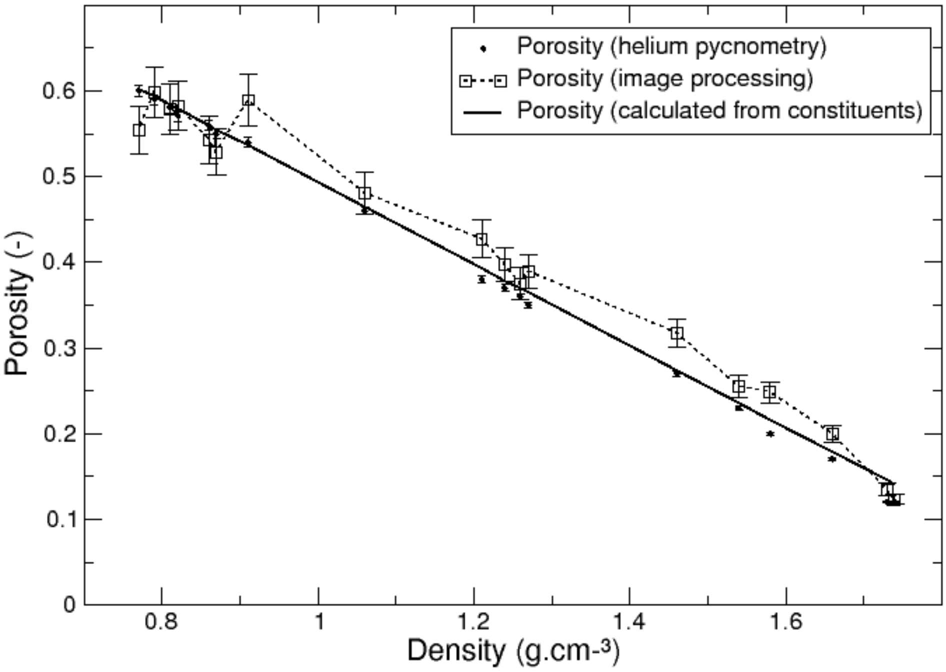

Figure 12: Comparison between calculated, experimental and theoretical porosities

numerical values are inferior to the experimental ones and this difference seems to decrease with the extent of infiltration. That could be explained by the presence of many microporosities between fibers before densification that progressively ~~decreases~~disappear as the pyrocarbon deposit grows.

The numerical internal surface area is underestimated due the limited resolution of the 3D μ-CT images, (8 µm/voxel): any detail inferior to 8 µm is not visible. The maximum internal surface area measurable by this method has been calculated from image resolution and the value is much lower than experimental measurements data (Fig.13). The same evolution had been found in a previous work [46] but with less differences between experimental and numerical values.

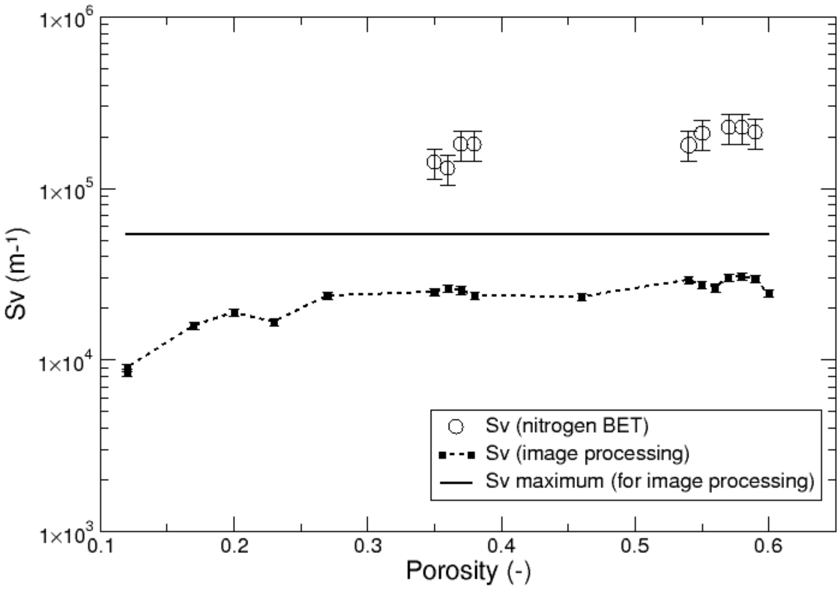

Figure 13: Comparison between calculated, experimental and maximum computed surface area

This may be due to the use of another gas (krypton, instead of N_2 here) for BET measurements.

Since the porosity and the internal surface area have been computed, it is possible to study the correlation between these quantities and compare it to formulæobtained from ideal structures (Fig. 14). Tomadakis and Sotirchos suggested to use the following equation for random arrays of freely overlapping cylinders of diameter d_f [37]:

$$S_v = \frac{-4\varepsilon \ln \varepsilon}{d_f} \tag{58}$$

For a value of d_f = 60 µm, the numerical results ~~fit~~agree well with the model for randomly overlapping cylinders in the middle range of porosity ($0.27 < \varepsilon < 0.46$), but they are underestimated for the lowest porosities or overestimated for

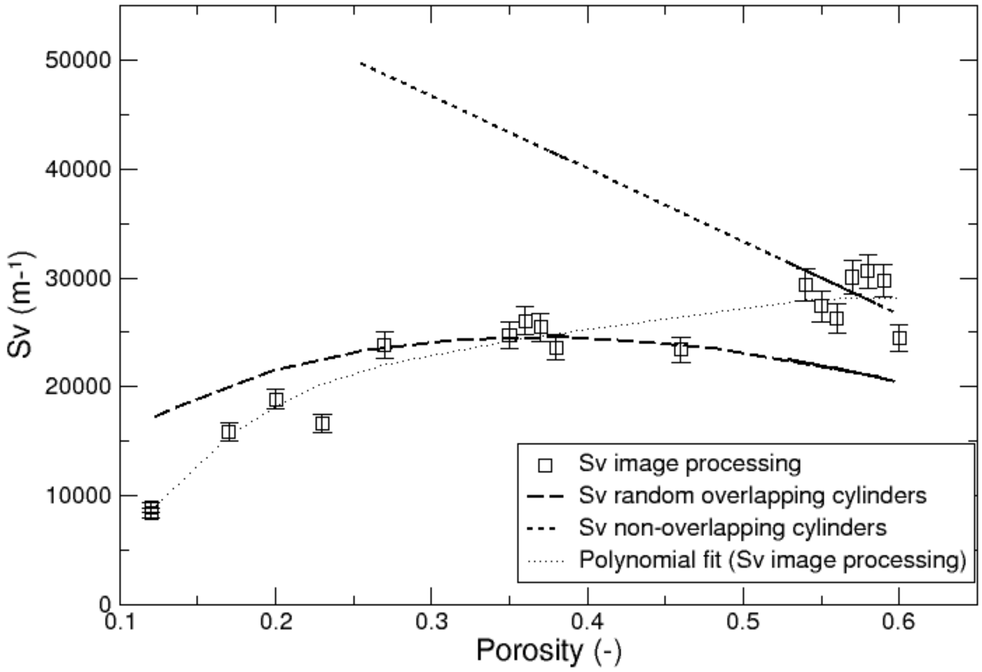

Figure 14: Comparison between calculated surface area and ideal media models

the highest porosities (Fig. 14). These differences can be explained by the complexity of the fibre arrangement in real materials. For less densified materials, that is, for the highest porosities, a better fit seems from Fig.14 to be achieved with the model for non-overlapping cylinders [38]:

$$S_v = \frac{4(1-\varepsilon)}{d_f} \tag{59}$$

These results are representative ~~to~~of the real preforms, because before the matrix deposition all the fibers do not overlap each other. For less porous materials, the error made in calculating the specific surface area is greatly increased because the pore size is getting closer to the voxel size. A polynomial fit on numerical values gives the following relationship :

$$S_v = -1.36 \cdot 10^6 \varepsilon^4 + 2.32 \cdot 10^6 \varepsilon^3 - 1.47 \cdot 10^6 \varepsilon^2 + 4.31 \cdot 10^5 \varepsilon - 2.56 \cdot 10^4 \quad (60)$$

This expression suggests the existence of a percolation porosity ε_p around 7%.

5.1.3. Average pore diameter

The experimental pore diameter distribution of four materials with distinct porosities were obtained from mercury porosimetry to assess changes in pore size during the densification process. Results are presented as incremental volume per unit mass of sample on Fig. 15.

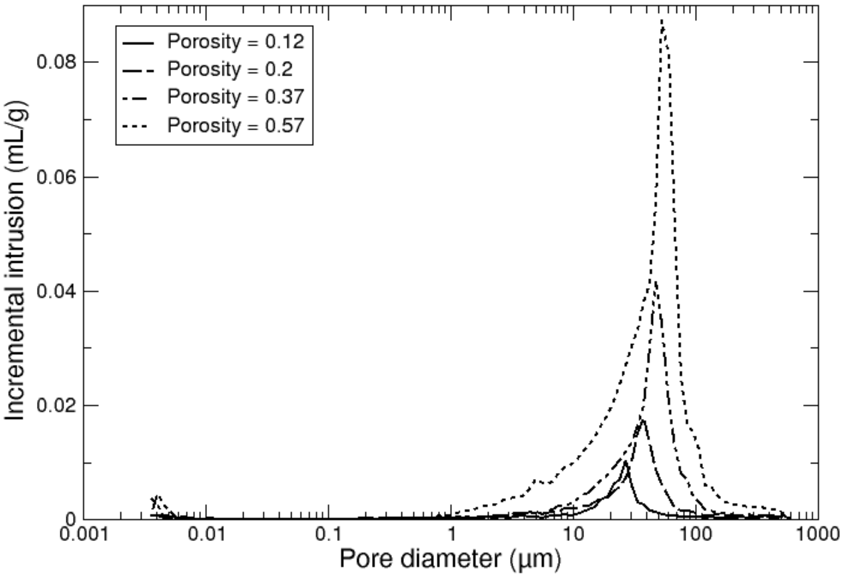

Figure 15: Pore diameter distributions measured by mercury porosimetry for samples with different porosities

For the least dense material, the maximum porous volume is reached for pores of 54 µm of diameter with a population that extends over several tens of µm.

This pores family represents 90-95% vol. of the detected pores. The denser the materials, the more the porous volume decreases, with a maximum reached for smaller pore diameters. The least dense material also has another pore family having diameters of the order of several nanometers. These pores are not visible on the tomographic images, which confirms the origin of the differences between the geometric values calculated on images and the measured ones.

Numerical results are compared with experimental ones for several samples with different porosities. Fig. 16 shows that there is a non negligible difference between mean pore chord lengths and mean pore diameters for the same reason as for the internal surface area : some micro-pores inferior to 8 µm, that are measured by mercury porosimetry (see Fig 15), are not detected ~~numerically~~in μ-CT scans due to insufficient image resolution.

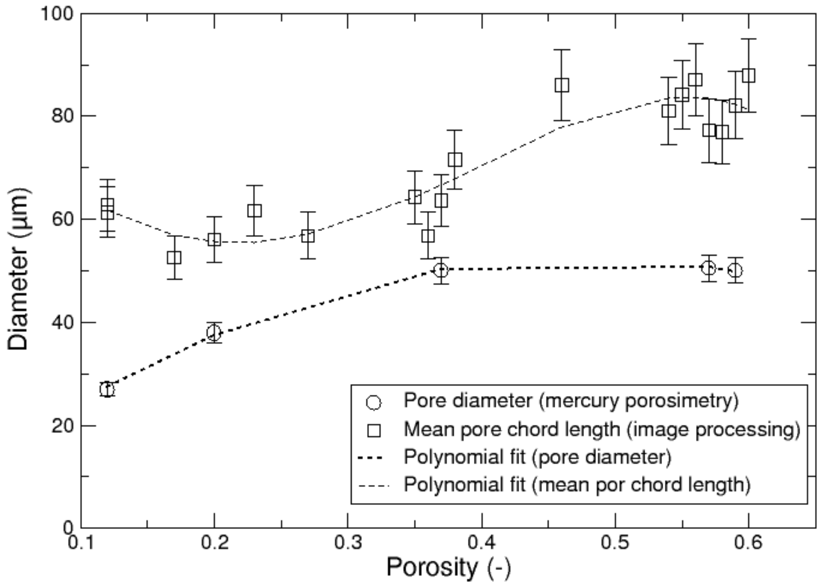

Figure 16: Comparison between calculated chord length in pores and mean pore diameter measured by Hg porosimetry

5.1.4. Average solid chord diameter

Mean chord length calculations can also be performed in the solid phase in order to estimate an equivalent solid diameter made of fibers and matrix Fig. 17. After fitting the curve, a good correlation between the mean solid chord length and porosity is observed :

$$\langle l_s \rangle = 39.74\varepsilon^{-1.2} \tag{61}$$

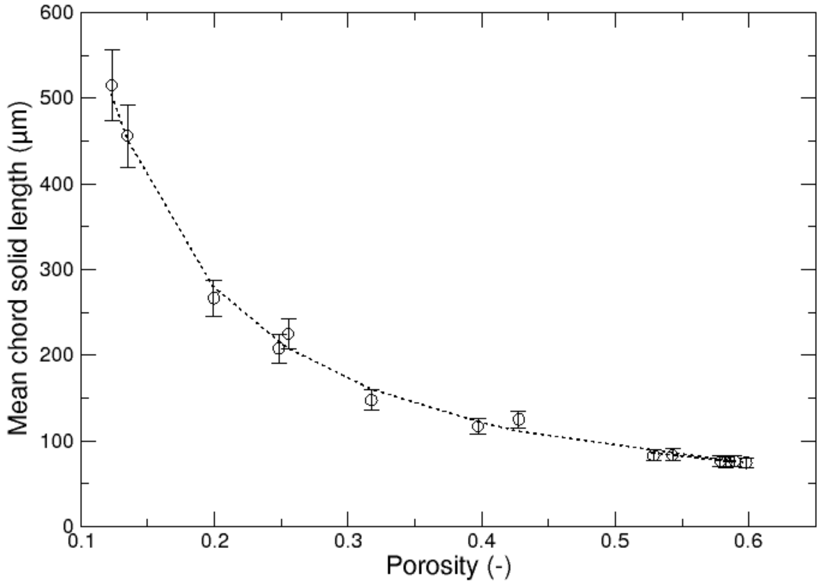

Figure 17: Mean calculated chord length in solid *vs.* porosity

As shown in chapter 3.2, models of literature concerning filters are focused on the fiber diameters and not on pore diameters. It could be interesting to find a correlation between the mean ~~solid~~ chord length in the solid and that in the pores to use it in these models. Eq. (46) already gives a correlation between fiber diameter ans pore diameter :

$$\frac{\phi \left\langle d_p \right\rangle}{\varepsilon \left\langle d_f \right\rangle} = 1 \tag{62}$$

To verify this relation, the equation (62) is calculated for all the materials using the mean solid chord length $\langle l_s \rangle$ as $\left\langle d_f \right\rangle$ and the mean pore chord length $\left\langle l_p \right\rangle$ as $\left\langle d_p \right\rangle$. Results are shown in Fig. 18: the ratios are not equal to 1 but to an average value of 0.8. From now on, for our materials, we can relate $\left\langle d_f \right\rangle$ to $\left\langle d_p \right\rangle$ with this relation :

$$\left\langle d_f \right\rangle \approx \frac{\phi \left\langle d_p \right\rangle}{0.8\varepsilon} \tag{63}$$

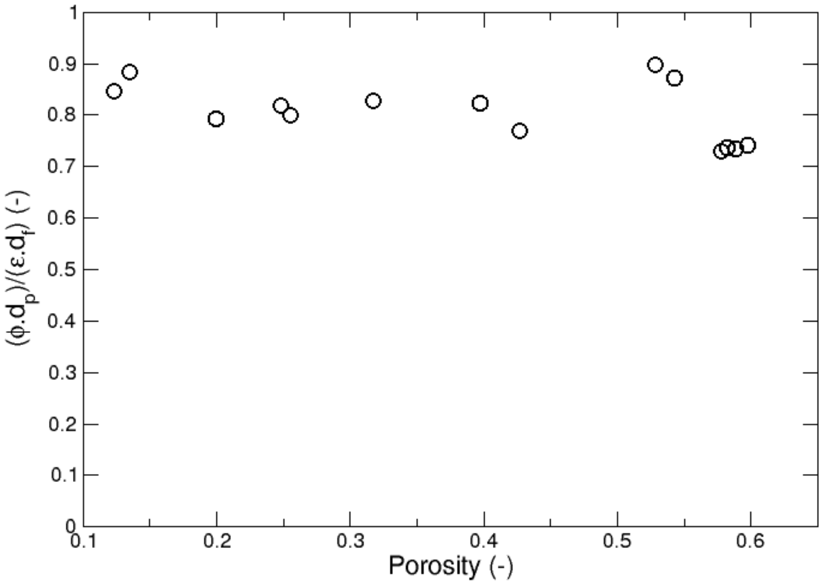

Figure 18: Comparison between mean calculated chord length in pores and in solid

5.2. *Knudsen diffusivity*

Comparisons between the experimental Knudsen diffusion coefficients and the simulated ones in the three directions of the samples are shown in figure 19; some observations can be made. As expected, Knudsen diffusion coefficients increase with porosity because more space is available for gas diffusion. Due to the presence of a greater macroporosity between the fiber mats, Knudsen diffusivities are lower in the transverse direction than in the in-plane direction.

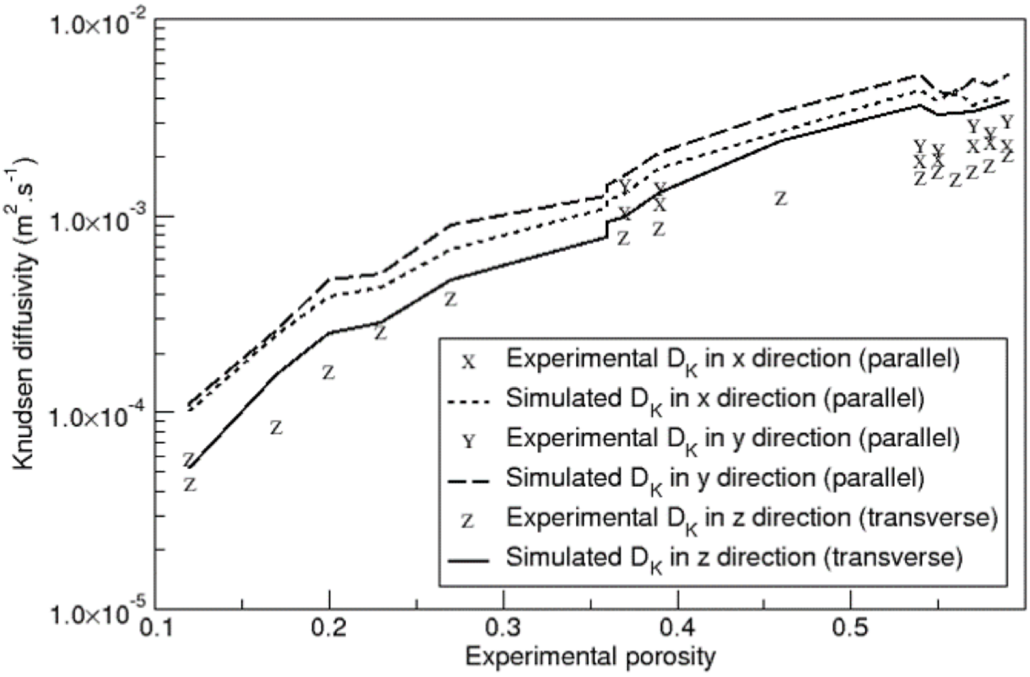

Figure 19: Comparison between simulated and experimental Knudsen diffusivities in each direction

Experimental and computed results were found in very close agreement considering numerical uncertainties (of the order of 10%). Discrepancies are more pronounced for highest porosities (Fig. 20). This problem is related to the geometrical details of the porous media. When materials are less densified they contain more micro-pores or isolated fibers that are not correctly detected by μ-

CT because of the image resolution (8µm/voxel) leading to an overestimation of the calculated diffusivity.

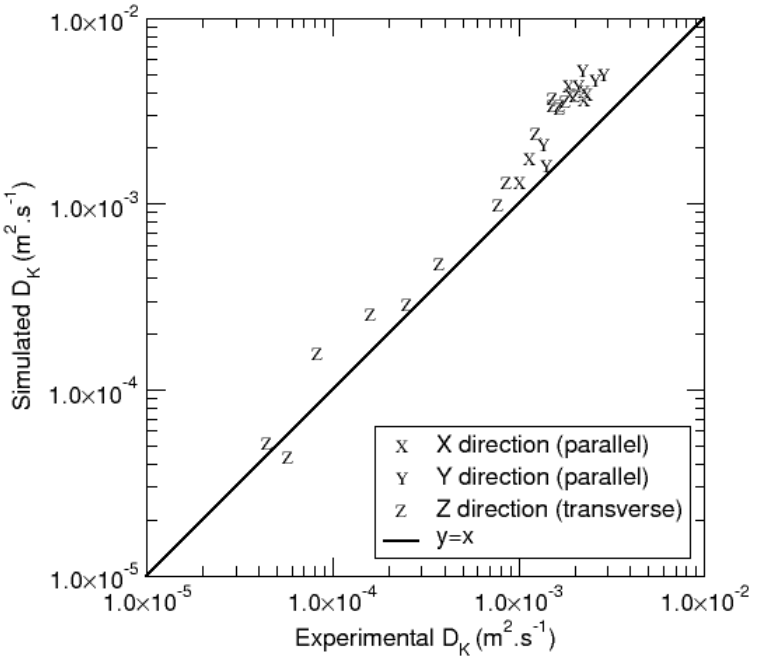

Figure 20: Relation between simulated and experimental Knudsen diffusivities

5.3. Viscous flow permeability

Computations have been performed both with the “direct” and the “indirect” method. The FV code PeSto was used for direct computations but, due to the importance of the computer resource and time needed to achieve the calculations, only few data points were produced. On the other hand, the MC/RW computations are very fast and their results can be exploited as indicated by Tomadakis & Robertson [26] and already verified previously by our team [44]. The model uses equations from Johnson *et al.* [27] concerning originally electrical transport. In this model, the permeability in a given eigen-direction j is related to a characteristic geometric parameter of the porous media, Λ, and to a formation factor F_j, defined as a relative resistance to transport through the porous media :

$$K_j = \frac{\Lambda_j^2}{8F_j} \tag{64}$$

Johnson *et al.* [27] relate Λ_j to mean pore diameter $\left\langle d_p \right\rangle$, porosity and form factor as :

$$\Lambda_j = -\frac{\left\langle d_p \right\rangle}{2} \left(\frac{\partial \ln F_j}{\partial \ln \varepsilon} \right)^{-1} \tag{65}$$

The formation factor F_j depends on the tortuosity in the binary diffusion regime and the porosity :

$$F_j = \frac{\mathcal{D}_b^{\mathrm{ref}}}{\mathcal{D}_{b,j}^{\mathrm{eff}}} = \frac{\eta_{b,j}}{\varepsilon} \tag{66}$$

Combining these relationships with the definition of tortuosity in viscous regime, one has [44] :

$$\eta_{v,j} = \frac{\eta_{b,j}}{M} . \left(1 - \frac{\partial \ln \eta_{b,j}}{\partial \ln \varepsilon} \right)^2 \tag{67}$$

with $M = 0.95$ [44].

The variations of the binary and Knudsen tortuosities with porosity were very satisfactorily fitted to the extended Archie's law Eq. (17). To verify this, the binary tortuosities obtained from direct computation are compared with the relation (17) for $\varepsilon_0 = 0.76$ and $\varepsilon_p = 0.07$ in figure 21. Table 4 summarizes the numerical values of the identified coefficients for all directions. The valuse of the exponents are in line with those published by Tomadakis & Sotirchos [98] and with recent evaluations made on computer-generated fibrous media designed to simulate fibrous fungi [99], for which $\alpha_b \approx 0.76$.

Table 4: Identified coefficients

Direction j	$\eta_j^{\lim}$	$\alpha_{b,j}$
x	1.566	0.559
y	1.227	0.620
z	1.420	0.776

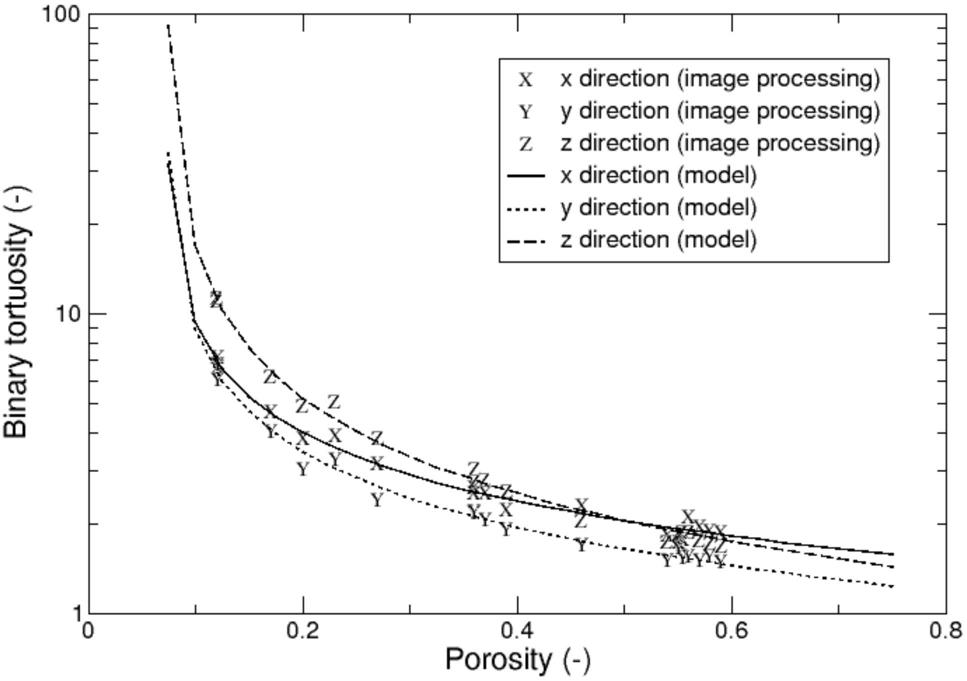

Figure 21: Relationship between computed binary tortuosity and porosity, compared with Tomadakis model (Eq. 17). The symbol sizes represent the amount of uncertainty.

Making use of relation (67), the viscous flow tortuosity is readily computed [44]:

$$\eta_{v,j} = \frac{\eta_{b,j}}{M} \cdot \left(1 + \frac{\alpha_{b,j}\varepsilon}{\varepsilon - \varepsilon_p}\right)^2 \tag{68}$$

This relation indicates that viscous and binary diffusion tortuosities are close to being proportional, except when the porosity decreases and becomes close to the percolation threshold value, in which case the viscous tortuosity increases much faster than the binary diffusion one.

Viscous tortuosities obtained by this method are compared with experimental and direct computations values in figure 22. The agreement between all values is very satisfactory, considering the experimental margins of uncertainty. The agreement between direct and indirect computations is excellent at low porosities, when convergence times are faster.

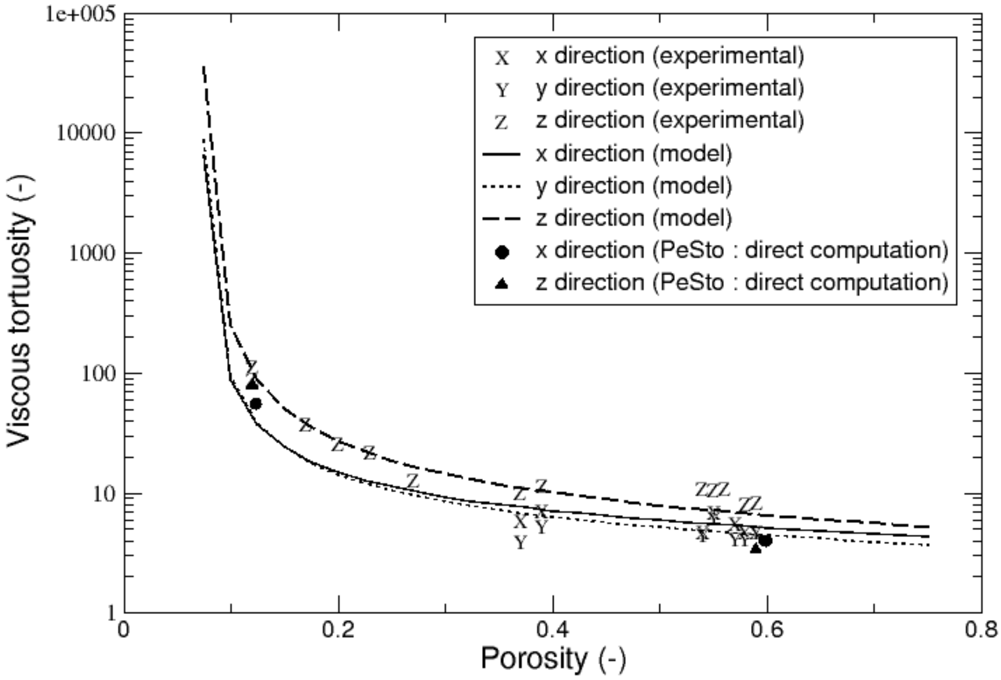

Figure 22: Calculated and experimental values of viscous tortuosity compared with Tomadakis's model (eq. 68)

Once again, the Tomadakis method has been found to be particularly suitable for describing the studied composites. Permeability estimates are easily obtained from CT data of a family of porous media by calculation of the binary tortuosity coefficients.

6. Discussions

6.1. Comparison with existing models and correlations : permeability

For sake of comparison, the permeability coefficient is often divided by the fiber diameter in order to have a dimensionless value. For densified materials studied here, an equivalent diameter comprising the fibers plus the matrix must be taken into account. Here, the computed average solid chord length is chosen as a reference diameter.

Results were compared with several numerical, experimental and theoretical data of 2D fiber mats extracted from the literature presented in section 3 (Fig. 24). Permeability measurements are in good agreement with others models or experimental data. However, it is noted that, in many publications, the permeability is experimentally obtained for porosities greater than 0.6, which is higher than the samples studied here. The differences between several models could be explained by the complexity of the fiber arrangements. Van Doormaal and Pharoah [59] highlight this fact by studying different fiber arrangements in which the angle between fibers in neighboring UD layers is a value between 0 and 90°. The results obtained by Shih & Lee (experimental permeability measurements on fiberglass mats) [65] and by Van Doormaal & Pharoah (calculations on 2D structures [59], with an angle of 60° between fibers) seem to best fit our results for in-plane flow. In contrast, our permeabilities are lower than those of Tomadakis [26] on randomly oriented fibers, as could be expected.

In through-thickness flow experiments, the whole section of the material contains fibers placed perpendicularly to the flow direction. For in-plane flow, this is not the case for regions containing fibers lying parallel to the flow direction.

Consequently, the values are more scattered in the latter situation, due to a larger sensitivity to the precise fibrous arrangement. Our results are in excellent alignment with existing data ~~for~~at porosity values ~~in~~for which comparison is possible; otherwise, the tendencies obtained at low porosity in this work seem to provide a consistent extension of the tendencies previously described in literature. Some differences may occur because most of the fibrous models consider non-densified media with non-overlapping fibers whereas in our case “fibers” are partially overlapping.

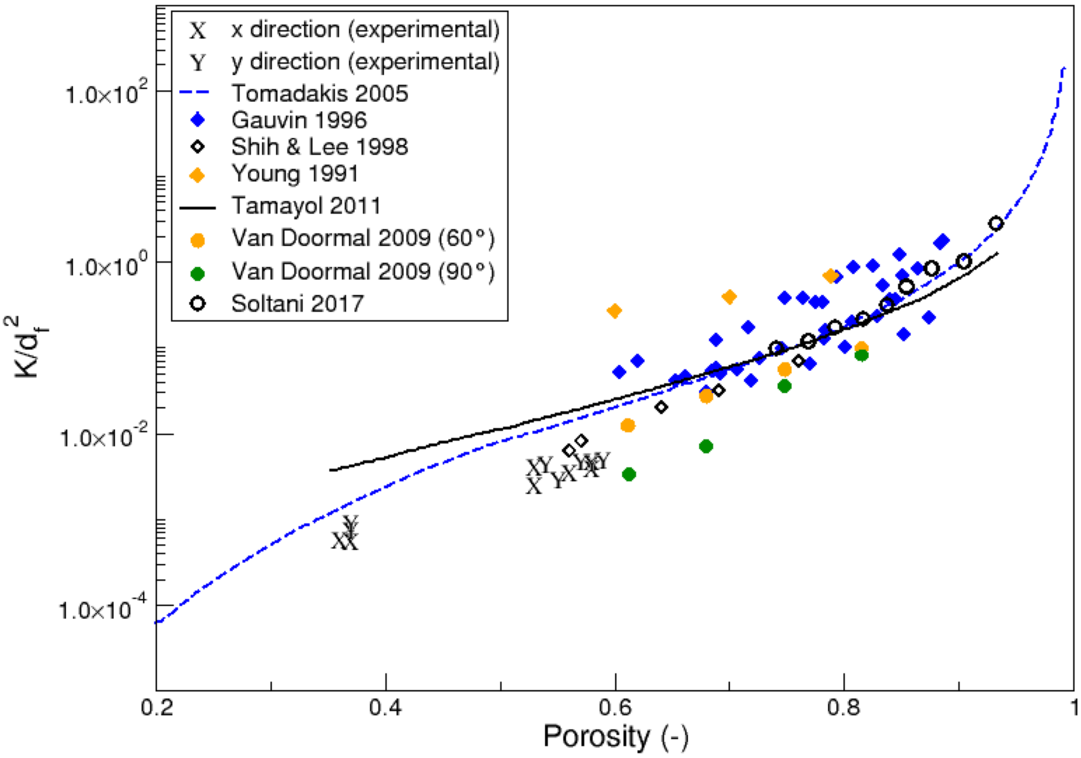

Figure 23: Permeability experimental results compared with literature : in-plane flow

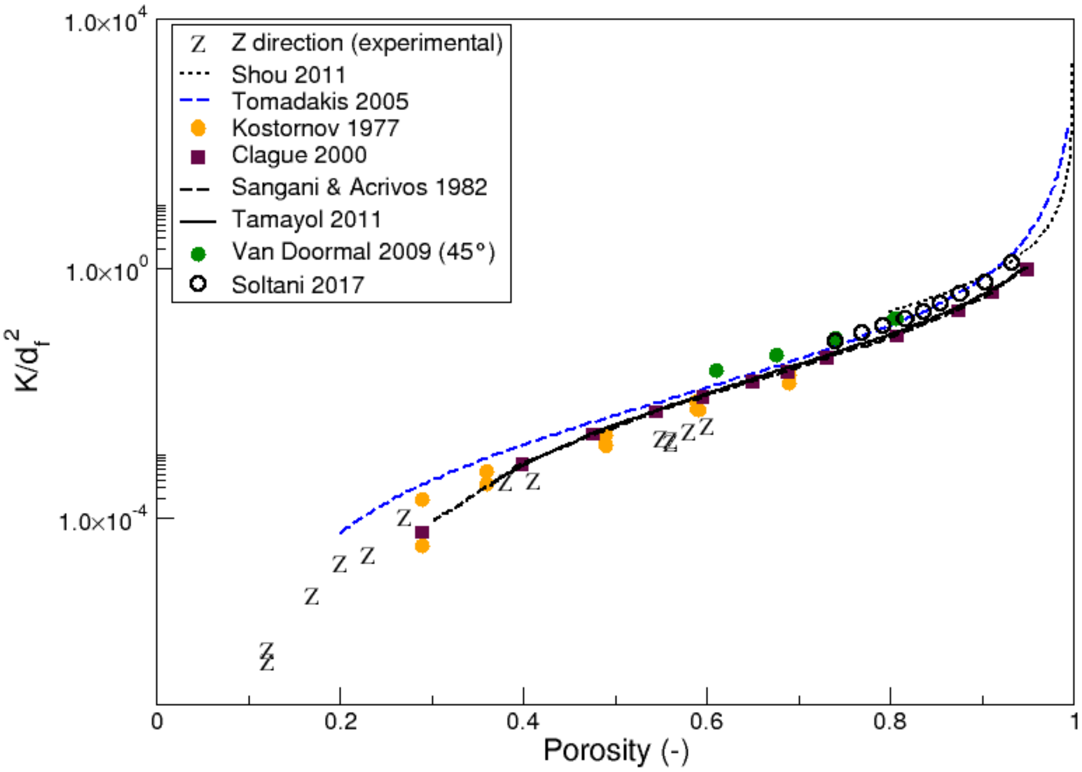

Figure 24: Permeability experimental results compared with literature : through-the-thickness flow

6.2. *Comparison with existing models and correlations : Knudsen diffusion*

Equation (44), presented in section 3.4, relates the evolution of the viscous flow considering rarefied or slip-flow regime.

Combining equation (44) with eqs. (15) and (63), it is possible to obtain an expression for the Knudsen transfer tortuosity:

$$\tau = 3.616\varepsilon^2\eta_K^{-1} \tag{69}$$

or:

$$\eta_K = 3.616\varepsilon^2\tau^{-1} \tag{70}$$

The evolution of the τ coefficient with porosity is compared with literature models of filters presented in Table. 3, figure 25. Results obtained in the present study are consistent with the tendencies given by Pich [70] and Yeh & Liu [69], whereas results from Kirsch [4] are scattered around the same tendency curves. Data from Pich [67] and Glushkov [68] are slightly higher but these models are given for a pure free-molecule regime and very high porosity values, which is not exactly the case for our study.

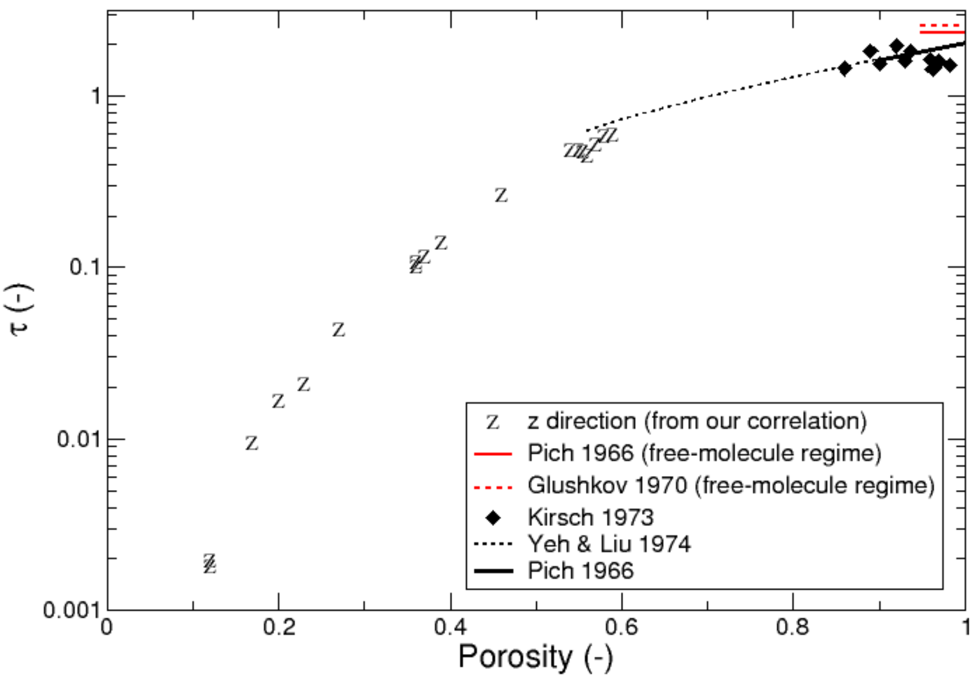

Figure 25: Evolution of factor τ (see eq. (44)) with porosity, and comparison with literature models on filters.

6.3. Correlations between transport modes

As suggested by Johnson & Koplik [27], then by Tomadakis & Robertson [26] and our team [44], and confirmed in the previous sections, correlations do exist between tortuosities for binary diffusion and for viscous flow. Indeed, by combining equation (21) and (17) we have :

$$\eta_{v,j} = \eta_{b,j} \left(1 + \frac{\alpha_{b,j} \left[\varepsilon_p + \left(\frac{\eta_{b,j}^{\lim}}{\eta_{b,j}} \right)^{1/\alpha_{b,j}} .(\varepsilon_0 - \varepsilon_p) \right]}{\left(\frac{\eta_{b,j}^{\lim}}{\eta_{b,j}} \right)^{1/\alpha_{b,j}} .(\varepsilon_0 - \varepsilon_p)} \right)^2 \tag{71}$$

To push further the investigation, we have also considered another type of fibrous medium: the Calcarb® material presented in section 4.2 in which numerical infiltrations have been achieved on the basis of two distinct CT scans.

The correlation between the experimental viscous tortuosity and the numerical binary tortuosity is compared with equation (71) on figure 26.

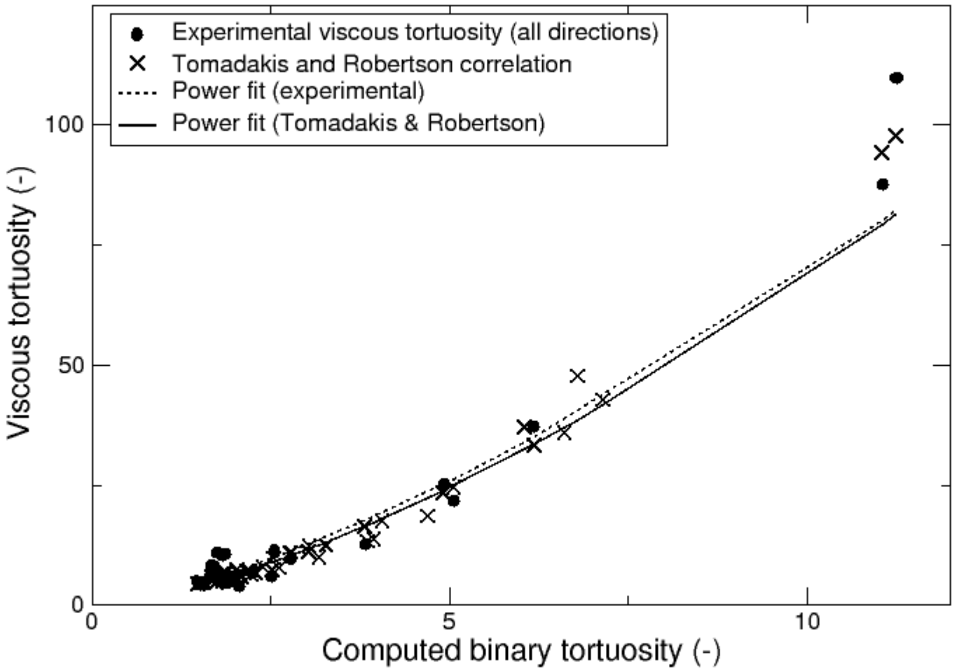

Figure 26: Correlation between viscous and computed binary tortuosities, comparison with Tomadakis correlation

Even if Calcarb® has a different microstructure, as compared to the 2.5D materials, the tendencies are very close to each other. Experimental values are in good agreement with those calculated from eq. (71). Additionally, it has been found that this expression can be replaced with a modest loss of accuracy by a simpler power law expression that can be written as :

$$\eta_v \approx 2.3\eta_b^{1.5} \tag{72}$$

The 1.5 exponent indicates that viscous transport is more sensitive than binary diffusion to the details of the porous medium geometry.

The next question is : is there also a correlation involving Knudsen tortuosities ? To answer it, we have collected Knudsen and binary diffusion tortuosity values in all directions and for all types of fibrous media investigated so far here. They were also compared with the η_b and η_K coefficients calculated from the extended Archie's law described in Eq. (17). The resulting plot is given in figure 27).

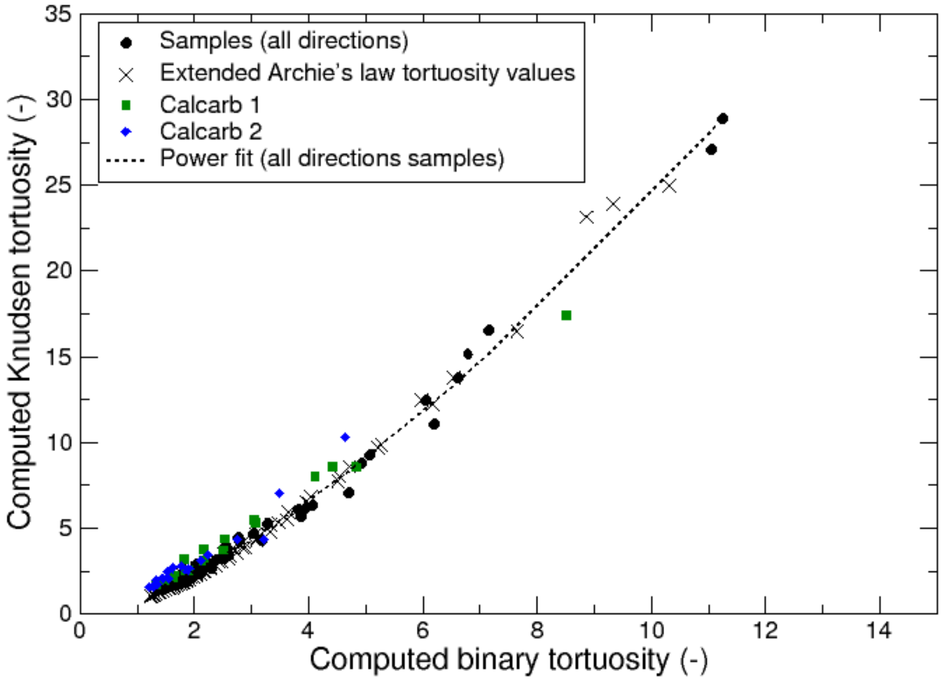

Figure 27: Correlation between calculated binary and knudsen tortuosities, comparison with calcarb and extended Archie's law values

The correlation between η_b and η_K also seems very similar. Moreover, the values from extended Archie's law model fit well with the computed ones. Fitting the experimental data with a power law, η_K could be related to η_b :

$$\eta_K \approx \eta_b^{1.43} \tag{73}$$

Here we see that Knudsen diffusion has approximately the same sensitivity to geometric details as the viscous tortuosity. Combining equations (73) and (72) leads to :

$$\eta_v \approx 2.3\eta_k^{1.05} \tag{74}$$

This relation is compared with experimental values of Knudsen and viscous experimental tortuosities in figure 28. Once again, the experimental values seem to follow the proposed correlation, except for porosities close to the percolation threshold ε_p where the viscous tortuosity increases rapidly. In this case the flow moves through increasingly thin passages, inducing much calculation error.

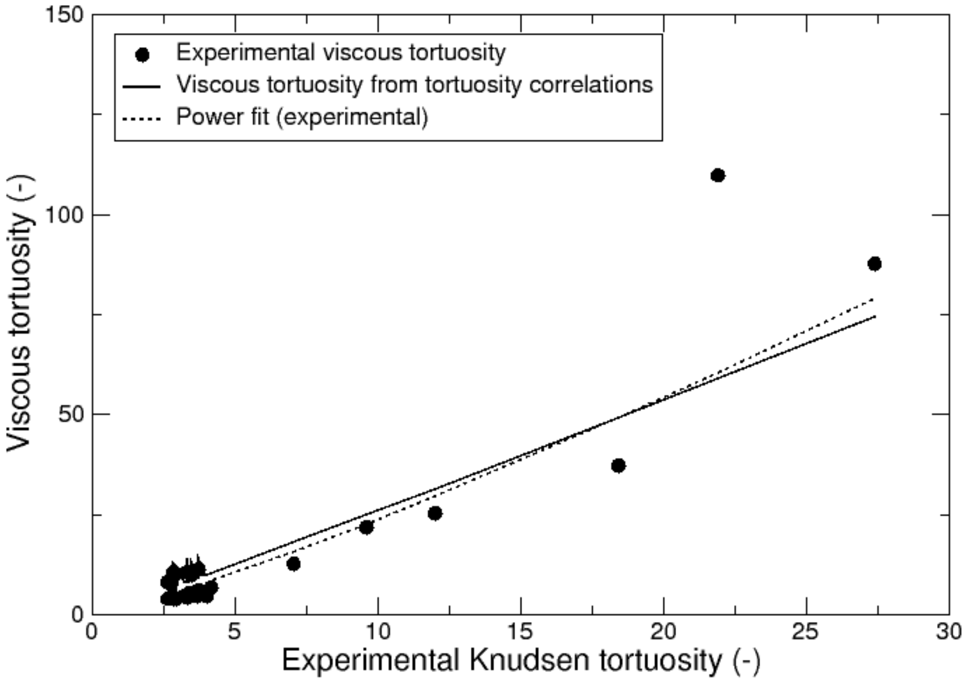

Figure 28: Correlation between viscous and Knudsen experimental tortuosities, comparison with earlier correlations from models

Summarizing the results, there is a clear correlation between the three kinds of gas transport for different kinds of fibrous materials. Remarkably, correlations are similar for different flow directions and for different kinds of fibrous media. This supports some degree of generality to these correlations, which can be very conveniently used in mass transfer modeling.

7. Conclusion

In this work, the geometrical and pure gas flow transfer properties of partly infiltrated fibrous preforms of C_f/C composites and of fibrous felts have been investigated both by X-ray μ-CT, image analysis and image-based computations on the one hand and by experimental techniques including density, BET surface area, Hg penetration and steady-state, low-pressure permeability measurements on the other hand. The main outcomes of the work are :

- Image-based and experimental pore size measurements are in good agreement;
- A simple correlation has been found between mean pore diameter and mean solid chord length;
- An excellent agreement has been found between experimental and μ-CT-derived values of Knudsen diffusivity and viscous permeability ;
- The indirect method proposed by Tomadakis & Robertson [26] for porous media families has been found once again to be efficient.

It is striking to note that the agreement is very good even though the μ-CT scans resolution did not allow ~~to~~ distinguishing individual fibers. A possible reason for this surprising success is that the sizes of the largest pores - which are most important for mass transfer - are well measured by the tomographic technique.

The results obtained in the frame of this study have been compared to literature data (experiments and computations) obtained mostly for fibrous filters with higher values of porosities. A very good match between them has been found; accordingly, this work proposes for the first time extensions of known correlations towards lower values of porosity. The key element allowing such an agreement is that we have used the mean solid chord length instead of the fiber diameter, the latter being the usual practice in filter science.

Finally, it has been found that the dimensionless friction factors (or tortuosities) related to Knudsen diffusion, binary diffusion and viscous flow are correlated between each other. The correlations are the same, regardless the flow direction, for neatly distinct types of fibrous media (*i.e.* partly infiltrated C_f/C composites preforms and fibrous felts). They are easy-to-use tools for large-scale numerical simulations of mixed-mode gas flow, *eg.* in Chemical Vapor Infiltration (CVI) or filter clogging simulations. A valuable outcome is the reduction of the number of experimental determinations of transport properties necessary for such a modeling frame: for instance, having information on Darcian permeability suffices to also provide information on Knudsen and binary diffusion in the same proous medium. Such a possibility relies on the determination of the mean solid chord length, which is accessible not only by μ-CT but also from the analysis of simple sectional micrographs, as is classical *eg.* in ceramics literature.

There are at least two directions for future work. First, it would be interesting to obtain experimental data on binary gas diffusion, using a modification of our setup with gas mixtures. Comparison to already computed diffusivities would strengthen the proposed approach. Second, transport properties linked to the solid phase could be studied, like electrical or thermal conduction. Indeed, Tomadakis & Sotirchos [100] had suggested that there exist relations between transport in the solid phase and in the void phase, following Keller's phase exchange theorem

[101]. Verifying these possible relationships in the case of intermediate-range porosities would bring new tools for multiphysics simulations in porous media.

Acknowledgements

Financial support to this work has been provided by ArianeGroup France to C. C. through a PhD grant. Authors are indebted to S. Couthures and T. Malard for help in developing the permeability measurement setup. X-ray μ-CT scans were obtained at the Placamat CNRS/Bordeaux University characterization service unit.

References

[1] M. Ondarts, L. Reinert, S. Guittonneau, S. Baup, S. Delpeux, J.-M. Lévêque, L. Duclaux. Improving the adsorption kinetics of ibuprofen on an activated carbon fabric through ultrasound irradiation: Simulation and experimental studies. *Chemical Engineering Journal*, 343:163–172, July 2018. `doi:10.1016/j.cej.2018.02.062`

[2] W. Szmyt, C. Guerra-Nùñez, C. Dransfeld, I. Utke. Solving the inverse Knudsen problem: Gas diffusion in random fibrous media. *Journal of Membrane Science*, 620:118728, February 2021. `doi:10.1016/j.memsci.2020.118728`

[3] P. Tronville, B. Zhou, R. Rivers. Realistic air filter media performance simulation. Part I: Navier–Stokes/finite-volume computational fluid dynamics procedures. *HVAC&R Research*, 19(5):493–502, July 2013. Publisher: Taylor & Francis `doi:10.1080/10789669.2013.795464`

[4] A. A. Kirsch, I. B. Stechkina, N. A. Fuchs. Effect of gas slip on the pressure

drop in fibrous filters. *Journal of Aerosol Science*, 4(4):287 – 293, 1973. `doi:10.1016/0021-8502(73)90089-X`

[5] R. Przekop, L. Gradoń. Deposition and Filtration of Nanoparticles in the Composites of Nano- and Microsized Fibers. *Aerosol Science and Technology*, 42(6):483–493, April 2008. Publisher: Taylor & Francis `doi:10.1080/02786820802187077`

[6] N. N. Mansour, F. Panerai, A. Martin, D. Y. Parkinson. A. MacDowell, A. Haboub, T. Dandstrom, T. Fast, G. Vignoles, J. Lachaud, A New Approach To Light-Weight Ablators Analysis: From Micro-Tomography Measurements to Statistical Analysis and Modeling. In *Procs. 44th AIAA Thermophysics Conference*, San Diego, CA, 24 - 27 June 2013, P. Yee editor, *AIAA Papers* 2013-2768 (11 p.), `doi:10.2514/6.2013-2768`

[7] F. Panerai, J. D. White, T. J. Cochell, O. M. Schroeder, N. N. Mansour, M. J. Wright, A. Martin. Experimental measurements of the permeability of fibrous carbon at high-temperature. *International Journal of Heat and Mass Transfer*, 101:267–273, 2016. `doi:10.1016/j.ijheatmasstransfer.2016.05.016`

[8] E. Stern, I. Nompelis, T. E. Schwartzentruber, G. V. Candler. Microscale Simulations of Porous TPS Materials: Application to Permeability. In *Procs. 11th AIAA/ASME Joint Thermophysics and Heat Transfer Conference*, AIAA AVIATION Forum, June 2014, *AIAA Papers* 2014-2247 (15 p.). `doi:10.2514/6.2014-2247`

[9] J. Marschall, F. S. Milos. Gas Permeability of Rigid Fibrous Refractory Insulations. *Journal of Thermophysics and Heat Transfer*, 12(4):528–535, 1998. `doi:10.2514/2.6372`

[10] D. Ehrlich, J. A. Schwille. Permeability of space vehicle fibrous thermal protection blankets in viscous and slip flow regimes. *Journal of Aerospace Engineering*, 28(3), 2015. `doi:10.1061/(ASCE)AS.1943-5525.0000418`

[11] J. Lu, H. K. Jang, S. B. Lee, W. R. Hwang. Characterization on the anisotropic slip for flows over unidirectional fibrous porous media for advanced composites manufacturing. *Composites Part A: Applied Science and Manufacturing*, 100:9–19, 2017. `doi:10.1016/j.compositesa.2017.04.021`

[12] D.-H. Shou, J.-T. Fan, M.-F. Mei, F. Ding. An analytical model for gas diffusion though nanoscale and microscale fibrous media. *Microfluidics and Nanofluidics*, 16(1):381–389, 2014. `doi:10.1007/s10404-013-1215-8`

[13] C. Chan, N. Zamel, X-G. Li, J. Shen. Experimental measurement of effective diffusion coefficient of gas diffusion layer/microporous layer in PEM fuel cells. *Electrochimica Acta*, 65:13–21, 2012. `doi:10.1016/j.electacta.2011.12.110`

[14] G. L. Vignoles. Chemical vapor deposition/infiltration processes for ceramic composites. In *Advances in Composites Manufacturing and Process Design*, P. Boisse, editor, chapter 8, pages 147–176. Elsevier Woodhead Publishing, 2015. `doi:10.1016/B978-1-78242-307-2.00008-7`

[15] R. R. Melkote, K. F. Jensen. Gas diffusion in random-fiber substrates. *AIChE Journal*, 35(12):1942–1952, 1989. `doi:10.1002/aic.690351205`

[16] H.-J. Li, X.-H. Hou, Y.-X. Chen. Densification of unidirectional carbon–carbon composites by isothermal chemical vapor infiltration. *Carbon*, 38(3):423–427, 2000. `doi:10.1016/S0008-6223(99)00122-0`

[17] B. Karakashov, J. Toutain, F. Achchaq, P. Legros, V. Fierro, A. Celzard. Permeability of fibrous carbon materials. *Journal of Materials Science*, 54(21):13537–13556, 2019. `doi:10.1007/s10853-019-03854-5`

[18] G. L. Vignoles. Modeling of chemical vapor infiltration processes. In *Advances in Composites Manufacturing and Process Design*, P. Boisse, editor, chapter 17, pages 415–458. Elsevier Woodhead Publishing, 2015. `doi:10.1016/B978-1-78242-307-2.00017-8`

[19] P.-C. Gervais, S. Bourrous, F. Dany, L. Bouilloux, L. Ricciardi. Simulations of filter media performances from microtomography-based computational domain. Experimental and analytical comparison. *Computers and Fluids*, 116:118–128, 2015. `doi:10.1016/j.compfluid.2015.04.019`

[20] P.-C. Gervais, D. Bémer, S. Bourrous, and L. Ricciardi. Airflow and particle transport simulations for predicting permeability and aerosol filtration efficiency in fibrous media. *Chemical Engineering Science*, 165:154–164, 2017. `doi:10.1016/j.ces.2017.03.002`

[21] H. M. Fu. Pressure drop and permeability of three-dimensional virtual fibrous medium. *Materials Research Innovations*, 19:S1421–S1427, 2015. `doi:10.1179/1432891715Z.0000000001584`

[22] S. Woudberg, F. Theron, E. Lys, L. Le Coq. Investigating the influence of local porosity variations and anisotropy effects on the permeability of fibrous media for air filtration. *Chemical Engineering Science*, 180:70–78, 2018. `doi:10.1016/j.ces.2018.01.035`

[23] M. Rojas-Cárdenas, E. Silva, M.-T. Ho, C. J. Deschamps, I. Graur. Time-dependent methodology for non-stationary mass flow rate measurements in

a long micro-tube. *Microfluidics and Nanofluidics*, 21(5):86, 2017. `doi:10.1007/s10404-017-1920-9`

[24] M. V. Johansson, F. Testa, I. Zaier, P. Perrier, J. P. Bonnet, P. Moulin, I. Graur. Mass flow rate and permeability measurements in microporous media. *Vacuum*, 158:75–85, 2018. `doi:10.1016/j.vacuum.2018.09.030`

[25] Y. Hou, S. Comas-Cardona, C. Binetruy, and S. Drapier. Gas transport in fibrous media: Application to in-plane permeability measurement using transient flow. *Journal of Composite Materials*, 47(18):2237–2247, 2013. `doi:10.1177/0021998312455676`

[26] M. M. Tomadakis, T. J. Robertson. Viscous Permeability of Random Fiber Structures: Comparison of Electrical and Diffusional Estimates with Experimental and Analytical Results. *Journal of Composite Materials*, 39(2):163–188, 2005. `doi:10.1177/0021998305046438`

[27] D. L. Johnson, J. Koplik, L. M. Schwartz. New Pore-Size Parameter Characterizing Transport in Porous Media. *Physical Review Letters*, 57(20):2564–2567, November 1986. `doi:0.1103/PhysRevLett.57.2564`

[28] G. L. Vignoles, P. Charrier, C. Preux, B. Dubroca. Rarefied Pure Gas Transport in Non-isothermal Porous Media: Effective Transport Properties from Homogenization of the Kinetic Equation. *Transport in Porous Media*, 73(2):211–232, June 2008. `doi:10.1007/s11242-007-9167-7`

[29] B. Ghanbarian, A. G. Hunt, P. P. Ewing, M. Sahimi. Tortuosity in Porous Media: A Critical Review. *Soil Science Society of America Journal*, 77(5):1461, 2013. `doi:10.2136/sssaj2012.0435`

[30] M. B. Clennell. Tortuosity: a guide through the maze. In *Development in Petrophysics*, M. A. Lovell, P. K. Harvey, editors, *Geological Society, London, Special Publications*, 122(1):299–344, 1997. `doi:10.1144/GSL.SP.1997.122.01.18`

[31] S. Roy, R. Raju, H. F. Chuang, B. A. Cruden, M. Meyyappan. Modeling gas flow through microchannels and nanopores. *Journal of Applied Physics*, 93(8):4870–4879, 2003. `doi:10.1063/1.1559936`

[32] L. J. Klinkenberg. The permeability of porous media to liquids and gases. In*Drilling and Production Practices*, American Petroleum Institute, 1941, pp. 200-213. `https://onepetro.org/APIDPP/proceedings-abstract/API41/All-API41/API-41-200/52076`

[33] M. M. Tomadakis, S. V. Sotirchos. Ordinary, transition, and Knudsen regime diffusion in random capillary structures. *Chemical Engineering Science*, 48(19):3323–3333, 1993. `doi:10.1016/0009-2509(93)80149-K`

[34] M. M. Tomadakis, S. V. Sotirchos. Ordinary and transition regime diffusion in random fiber structures. *AIChE Journal*, 39(3):397–412, 1993. `doi:10.1002/aic.690390304`

[35] V. N. Burganos, S. V. Sotirchos. Knudsen Diffusion in parallel, multidimensional or randomly oriented capillary structures. *Chemical Engineering Science*, 44(11):2451–2462, 1989. `doi:10.1016/0009-2509(89)85189-9`

[36] S. V. Sotirchos, M. M. Tomadakis. Modelling Transport, Reaction, and Pore Structure Evolution During Densification of Cellular or Fibrous Structures. In *Chemical Vapor Deposition of Refractory Metals and Ceramics*,

T. M. Besmann, D. Gallois, editors, *MRS Online Proceedings Library Archive*, 168:73–78, 1989. `doi:10.1557/PROC-168-73`

[37] M. M. Tomadakis, S. V. Sotirchos. Effective Kundsen diffusivities in structures of randomly overlapping fibers. *AIChE Journal*, 37(1):74–86, 1991. `doi:10.1002/aic.690370107`

[38] M. M. Tomadakis, S. V. Sotirchos. Knudsen diffusivities and properties of structures of unidirectional fibers. *AIChE Journal*, 37(8):1175–1186, 1991. `doi:10.1002/aic.690370807`

[39] G. E. Archie. The electrical resistivity log as an aid in determining some reservoir characteristics. *Transactions of the AIME* 146(1):54-62, 1942. `doi:10.2118/942054-G`

[40] R. R. Melkote, K. F. Jensen. Computation of transition and molecular diffusivities in fibrous media. *AIChE Journal*, 38(1):56–66, 1992. `doi:10.1002/aic.690380106`

[41] G. L. Vignoles. Modelling Binary, Knudsen and Transition Regime Diffusion Inside Complex Porous Media. *Journal de Physique IV*, 05(C5):C5–159–C5–166, 1995. `doi:10.1051/jphyscol:1995517`

[42] F. Transvalidou, S. V. Sotirchos. Effective diffusion coefficients in square arrays of filament bundles. *AIChE Journal*, 42(9):2426–2438, 1996. `doi:10.1002/aic.690420904`

[43] T. L. Starr. Gas transport model for chemical vapor infiltration. *Journal of Materials Research*, 10(9):2360–2366, 1995. `doi:10.1557/JMR.1995.2360`

[44] G. L. Vignoles, O. Coindreau, A. Ahmadi, D. Bernard. Assessment of geometrical and transport properties of a fibrous C/C composite preform as digitized by x-ray computerized microtomography: Part II. Heat and gas transport properties. *Journal of Materials Research*, 22(6):1537–1550, 2007. `doi:10.1557/JMR.2007.0216`

[45] D. J. Skamser, D. P. Bentz, R. T. Coverdale, M. S. Spotz, N. Martys, H. Jennings, and D. L. Johnson. Calculation of the Thermal Conductivity and Gas Permeability in a Uniaxial Bundle of Fibers. *Journal of the American Ceramic Society*, 77(10):2669–2680, 1994. `doi:10.1111/j.1151-2916.1994.tb04660.x`

[46] O. Coindreau, G. L. Vignoles. Assessment of Geometrical and Transport Properties of a Fibrous C/C Composite Preform Using x-ray Computerized Micro-tomography: Part I. Image Acquisition and Geometrical Properties. *Journal of Materials Research*, 20(9):2328–2339, 2005. `doi:10.1557/jmr.2005.0311`

[47] E. A. Mason. *Gas Transport in Porous Media: The Dusty-gas Model*. *Chemical Engineering Monographs* 17; Amsterdam ; New York : Elsevier Scientific Pub. Co., 1983. ISBN 0-444-41296-6

[48] P. J. A. M. Kerkhof. A modified Maxwell-Stefan model for transport through inert membranes: the binary friction model. *The Chemical Engineering Journal and the Biochemical Engineering Journal*, 64(3):319–343, 1996. `doi:10.1016/S0923-0467(96)03134-X`

[49] I. Langmuir. Report on Smokes and Filters. Tech. Report 865 Serial No. 353 (PB 99669), National Defence Commission, Office of Scientific Research and Development, Washington, December 1942. Reprinted in

Atmospheric Phenomena, The Collected Works of Irving Langmuir with Contributions in Memoriam Including a Complete Bibliography of His Works, C. G. Suits, H. E. Way, editors, Pergamon, 1961, pp. 394-436. `doi:10.1016/B978-0-08-009362-8.50023-5`

[50] C. Y. Chen. Filtration of Aerosols By Fibrous Media. *Chemical Reviews*, 55(3):595–623, 1955. `doi:10.1021/cr50003a004`

[51] J. Happel. Viscous flow relative to arrays of cylinders. *AIChE Journal*, 5(2):174–177, 1959. `doi:10.1002/aic.690050211`

[52] J. E. Drummond, M. I. Tahir. Laminar viscous flow through regular arrays of parallel solid cylinders. *International Journal of Multiphase Flow*, 10(5):515–540, 1984. `doi:10.1016/0301-9322(84)90079-X`

[53] A. Tamayol, M. Bahrami. Parallel Flow Through Ordered Fibers: An Analytical Approach. *Journal of Fluids Engineering*, 132(114502), 2010. `doi:10.1115/1.4002169`

[54] S. Kuwabara. The Forces experienced by Randomly Distributed Parallel Circular Cylinders or Spheres in a Viscous Flow at Small Reynolds Numbers. *Journal of the Physical Society of Japan*, 14(4):527–532, 1959. `doi:10.1143/JPSJ.14.527`

[55] C. N. Davies. The Separation of Airborne Dust and Particles. *Proceedings of the Institution of Mechanical Engineers*, 167(1b):185–213, 1953. `doi:10.1177/002034835316701b13`

[56] A. Tamayol, M. Bahrami. Transverse permeability of fibrous porous media. *Physical Review E*, 83(4):046314, 2011. `doi:10.1103/PhysRevE.83.046314`

[57] J. Van der Westhuizen, J. Prieur Du Plessis. An attempt to quantify fibre bed permeability utilizing the phase average Navier-Stokes equation. *Composites Part A: Applied Science and Manufacturing*, 27(4):263–269, 1996. `doi:10.1016/1359-835X(95)00039-5`

[58] A. S. Sangani, A. Acrivos. Slow flow past periodic arrays of cylinders with application to heat transfer. *International Journal of Multiphase Flow*, 8(3):193–206, 1982. `doi:10.1016/0301-9322(82)90029-5`

[59] M. A. Van Doormaal, J. G. Pharoah. Determination of permeability in fibrous porous media using the lattice Boltzmann method with application to PEM fuel cells. *International Journal for Numerical Methods in Fluids*, 59(1):75–89, 2009. `doi:10.1002/fld.1811`

[60] D. S. Clague, B. D. Kandhai, R. Zhang, P. M. A. Sloot. Hydraulic permeability of (un)bounded fibrous media using the lattice Boltzmann method. *Physical Review E*, 61(1):616–625, 2000. `doi:10.1103/PhysRevE.61.616`

[61] D.-H. Shou, J.-T. Fan, F. Ding. Hydraulic permeability of fibrous porous media. *International Journal of Heat and Mass Transfer*, 54(17-18):4009–4018, 2011. `doi:10.1016/j.ijheatmasstransfer.2011.04.022`

[62] P. Soltani, M. Zarrebini, R. Laghaei, A. Hassanpour. Prediction of permeability of realistic and virtual layered nonwovens using combined application of X-ray μ-CT and computer simulation. *Chemical Engineering Research and Design*, 124:299–312, 2017. `doi:10.1016/j.cherd.2017.06.035`

[63] A. G. Kostornov, M. S. Shevchuk. Hydraulic characteristics and structure of porous metal fiber materials: II. Effects of porosity, thickness, and

differential pressure on the principal properties of permeable fiber materials. *Soviet Powder Metallurgy and Metal Ceramics*, 12(9):752–756, 1973. `doi:10.1007/BF00793986`

[64] R. Gauvin, F. Trochu, Y. Lemenn, L. Diallo. Permeability measurement and flow simulation through fiber reinforcement. *Polymer Composites*, 17(1):34–42, 1996. `doi:10.1002/pc.10588`

[65] C.-H. Shih, L. J. Lee. Effect of fiber architecture on permeability in liquid composite molding. *Polymer Composites*, 19(5):626–639, 1998. `doi:10.1002/pc.10136`

[66] W. B. Young, K. Rupel, K. Han, L. J. Lee, M. J. Liou. Analysis of resin injection molding in molds with preplaced fiber mats. II: Numerical simulation and experiments of mold filling. *Polymer Composites*, 12(1):30–38, 1991. `doi:10.1002/pc.750120106`

[67] J. Pich. Pressure characteristics of fibrous aerosol filters. *Journal of Colloid and Interface Science*, 37(4):912–917, 1971. `doi:10.1016/0021-9797(71)90372-9`

[68] Yu. M. Glushkov. Resistance of fibrous filters in a slip flow. *Journal of Applied Mechanics and Technical Physics*, 11(4):700–703, 1970. `doi:10.1007/BF00850864`

[69] H.-C. Yeh, B. Y. H. Liu. Aerosol filtration by fibrous filters-I. theoretical. *Journal of Aerosol Science*, 5(2):191–204, 1974. `doi:10.1016/0021-8502(74)90049-4`

[70] J. Pich. Pressure drop of fibrous filters at small Knudsen numbers. *Ann. Occup. Hyg.*, 9:23–27, 1966. `doi:10.1093/annhyg/9.1.23`

[71] H.-J. Choi, M. Kumita, T. Seto, Y. Inui, L. Bao, T. Fujimoto, Y. Otani. Effect of slip flow on pressure drop of nanofiber filters. *Journal of Aerosol Science*, 114:244–249, 2017. `doi:10.1016/j.jaerosci.2017.09.020`

[72] P. C. Carman. Fluid flow through granular beds. *Chemical Engineering Research and Design*, 75:S32–S48, 1997. `doi:10.1016/S0263-8762(97)80003-2`

[73] N. Epstein. On tortuosity and the tortuosity factor in flow and diffusion through porous media. *Chemical Engineering Science*, 44(3):777–779, 1989. `doi:10.1016/0009-2509(89)85053-5`

[74] M. A. Choi, M. H. Lee, J. Chang, S. J. Lee. Permeability modeling of fibrous media in composite processing. *Journal of Non-Newtonian Fluid Mechanics*, 79(2-3):585–598, 1998. `doi:0.1016/S0377-0257(98)00120-7`

[75] O. Rahli, L. Tadrist, M. Miscevic, R. Santini. Fluid Flow Through Randomly Packed Monodisperse Fibers: The Kozeny-Carman Parameter Analysis. *Journal of Fluids Engineering*, 119(1):188–192, March 1997. `doi:10.1115/1.2819107`

[76] B. R. Gebart. Permeability of Unidirectional Reinforcements for RTM. *Journal of Composite Materials*, 26(8):1100–1133, August 1992. `doi:10.1177/002199839202600802`

[77] T. G. Gutowski, Z. Cai, S. Bauer, D. Boucher, J. Kingery, S. Wineman. Consolidation Experiments for Laminate Composites. *Journal of Composite Materials*, 21(7):650–669, 1987. `doi:10.1177/002199838702100705`

[78] T. T. Nguyen, B. Indraratna. Hydraulic behaviour of parallel fibres under

longitudinal flow: A numerical treatment. *Canadian Geotechnical Journal*, 53(7):1081–1092, 2016. `doi:10.1139/cgj-2015-0213`

[79] T. T. Nguyen, B. Indraratna. The permeability of natural fibre drains, capturing their micro-features. *Proceedings of the Institution of Civil Engineers: Ground Improvement*, 170(3):123–136, 2017. `doi:10.1680/jgrim.16.00032`

[80] P. Olry. Process and apparatus for manufacturing axi-symmetrical three-dimensional structures. Patent US4621662A granted Nov. 11, 1986.

[81] S. Brunauer, P. H. Emmett, E. Teller. Adsorption of Gases in Multimolecular Layers. *Journal of the American Chemical Society*, 60(2):309–319, 1938. `doi:10.1021/ja01269a023`

[82] N. Otsu. A Threshold Selection Method from Gray-Level Histograms. *IEEE Transactions on Systems, Man, and Cybernetics*, 9(1):62–66, 1979. `doi:10.1109/TSMC.1979.4310076`

[83] G. L. Vignoles, M. Donias, C. Mulat, C. Germain, J.-F. Delesse. Simplified marching cubes: An efficient discretization scheme for simulations of deposition/ablation in complex media. *Computational Materials Science*, 50(3):893–902, 2011. `doi:10.1016/j.commatsci.2010.10.027`

[84] The Mersen company, *Calcarb ® CBCF 15-2000 data sheet*, `https://www.mersen.de/sites/germany/files/publications-media/3-gs-calcarb-grade-cbcf-15-2000-mersen.pdf` Web page consulted May 21, 2021.

[85] G. Vignoles, W. Ros, C. Mulat, O. Coindreau, C. Germain. Pearson random walk algorithms for fiber-scale modeling of Chemical Vapor Infiltration.

Computational Materials Science 50:1157–1168, 2011. `doi:10.1016/j.commatsci.2010.11.015`

[86] G. L. Vignoles. A hybrid random walk method for the simulation of coupled conduction and linearized radiation transfer at local scale in porous media with opaque solid phases. *International Journal of Heat and Mass Transfer*, 93:707–719, 2016. `doi:10.1016/j.ijheatmasstransfer.2015.10.056`

[87] A. Einstein. *Investigations on the theory of Brownian movement*. R Fürth, editor. A. W. Cowper, translator. Dover Publications, New York, N.Y., 1956. ISBN: 9780486603049. `http://users.physik.fu-berlin.de/~kleinert/files/eins_brownian.pdf`

[88] S. Chandrasekhar. Stochastic Problems in Physics and Astronomy. *Reviews of Modern Physics*, 15(1):1–89, 1943. `doi:10.1103/RevModPhys.15.1`

[89] I. C. Kim, S. Torquato. Determination of the effective conductivity of heterogeneous media by Brownian motion simulation. *Journal of Applied Physics*, 68(8):3892–3903, 1990. `doi:10.1063/1.346276`

[90] S. Torquato, I. C. Kim. Efficient simulation technique to compute effective properties of heterogeneous media. *Applied Physics Letters*, 55(18):1847–1849, 1989. `doi:10.1063/1.102184`

[91] E. Sánchez-Palencia. *Non-Homogeneous Media and Vibration Theory*. Lecture Notes in Physics, vol. 127. Springer-Verlag, Berlin Heidelberg, 1980. `doi:10.1007/3-540-10000-8`

[92] G Papanicolaou, A Bensoussan, J.-L. Lions. *Asymptotic Analysis for Periodic Structures. Studies in Mathematics and its Applications*, J.-L. Lions,

G. Papanicolaou, R. T. Rockafellar, editors, vol. 5, North Holland, Elsevier, 1978. ISBN: 9780080875262 `https://www.123library.org/ebook/id/40707/`

[93] S. Whitaker. Diffusion and dispersion in porous media. *AIChE Journal*, 13(3):420–427, 1967. `doi:10.1002/aic.690130308`

[94] A. Bourgeat, M. Quintard, S. Whitaker. Eléments de comparaison entre la méthode d'homogénéisation et la méthode de prise de moyenne avec fermeture (Comparison between homogenization theory and volume averaging method with closure problem). *C. R. Acad. Sci. Paris II: Mechanics*, 306:463—466, 1988. `https://gallica.bnf.fr/ark:/12148/bpt6k5664568n/f469.image.r=bourgeat?rk=21459;2`

[95] A. J. Chorin. A Numerical Method for Solving Incompressible Viscous Flow Problems. *Journal of Computational Physics*, 135(2):118–125, 1997. `doi:10.1006/jcph.1997.5716`

[96] H. A. van der Vorst. Bi-CGSTAB: A Fast and Smoothly Converging Variant of Bi-CG for the Solution of Nonsymmetric Linear Systems. *SIAM Journal on Scientific and Statistical Computing*, 13(2):631–644, 1992. `doi:10.1137/0913035`

[97] Y. Saad. *Numerical Methods for Large Eigenvalue Problems*. Classics in Applied Mathematics CL66. Society for Industrial and Applied Mathematics, 2011. `doi:10.1137/1.9781611970739`

[98] M M. Tomadakis, S. V. Sotirchos. Effects of fiber orientation and overlapping on Knudsen, transition, and ordinary regime diffusion in fibrous structures in Chemical Vapor Deposition of Refractory Metals and Ceram-

ics II, T. M. Besmann, B. M. Gallois, J. W. Warren, Eds., *Mater. Res. Soc. Symp. Proc.* 250: 221-226,1992. `doi:10.1557/PROC-250-221`

[99] S. Schmieder, H. Müller, L. Barthel, T. Friedrich, L. Niessen, V. Meyer, H. Briesen. Universal law for diffusive mass transport through mycelial networks *Biotechnology and Bioengineering* 118:930-943, 2021. `doi:10.1002/bit.27622`

[100] M. M. Tomadakis, S. V. Sotirchos. Transport properties of random arrays of freely overlapping cylinders with various orientation distributions. *The Journal of Chemical Physics*, 98(1):616–626, 1993. `doi:10.1063/1.464604`

[101] J. B. Keller. A theorem on the conductivity of a composite medium. *J. Math. Phys.*, 5:548–549, 1964. `doi:10.1063/1.464604`

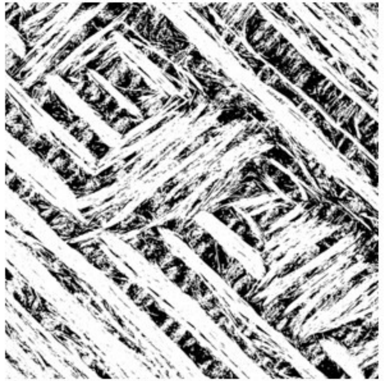

Fibrous C/C preforms

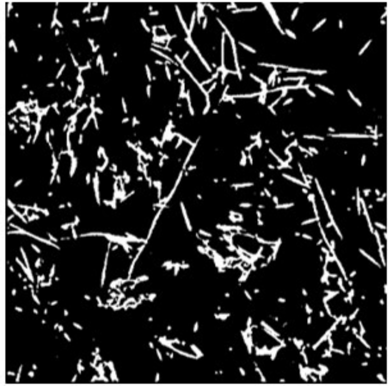

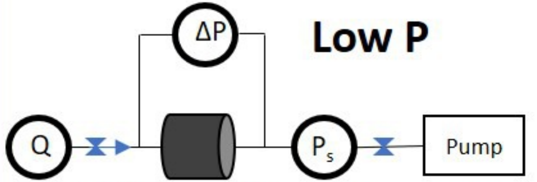

Flow/Pressure drop expts.

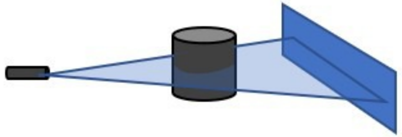

X-ray CT, Image analysis, Image-based computations

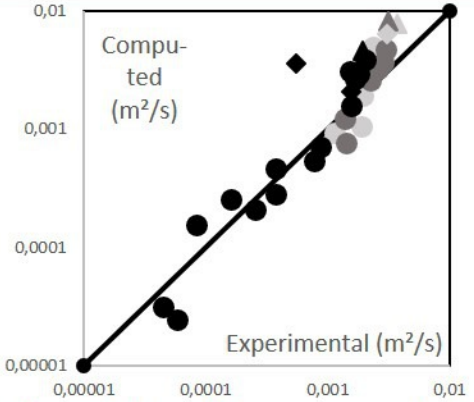

Good Exp/Comp. match

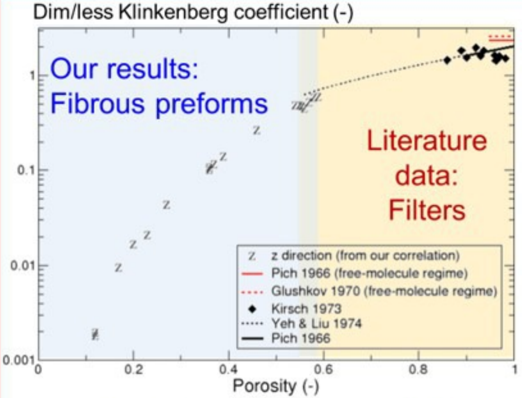

Consistent w/ data on filters

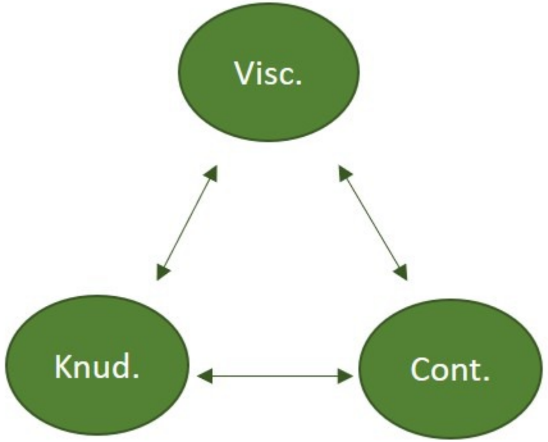

Correlations betw. transport modes